Chapter 4

SIW based Self-Multiplexed Antennas

Multi-frequency antennas for multi-standard applications are in high demand resulting from the rapid development of wireless communication services and systems [157]. Multiple transceivers are required in an RF (radio-frequency) frontend system for each application that has poor input isolation. In order to achieve improved isolation, highly selective multiplexers are constantly required, which expands the size of the system. Researchers are interested in the development of self-diplexing antennas because they reduce the need for higher-order diplexers, making the RF front-end system more compact, efficient, and cost-effective by decreasing the number of components. Self-diplexing antennas have been developed using a variety of methods [158]. Due to their high circuit size and design complexity, these antennas are not appropriate for small RF front-end devices. In past few years, substrate integrated waveguide (SIW) technology has emerged as a mature and promising candidate as it facilitates compact size, simple configuration, easy integration with RF front-end devices, good radiation characteristics and high unidirectional gain [159]. Specifically, it is really a challenging task to design a planar, miniaturized, low-cost self-diplexing antenna which has de-

sign simplicity and achieves low frequency ratio as well as high isolation between two operating bands throughout the operating range.

In this chapter, two novel designs are proposed to implement the self-multiplexing phenomenon in the SIW cavity-backed slot antenna topology, which helps to realize a compact integrated antenna multiplexer network while maintaining planar form and a simpler design configuration. This chapter is divided into two parts. First, a design of a SIW cavity-backed elliptical slot antenna is proposed to exhibit a self-diplexing antenna with two different operating frequencies for satellite and millimeter-wave 5G applications in section 4.1 . In section 4.2, a campact SIW cavity-backed non-linear replicated (NLR) hybrid slot antenna is proposed to implement the self-triplexing phenomenon.

4.1 A Dual-band Dual-Sense Circularly Polarized Self-Diplexing SIW Cavity-Backed Antenna with Elliptical Slot for Millimeter-Wave 5G Applications

In this section, a cavity-backed SIW antenna capable of supporting dual-band dual-sense CP operation is proposed for satellite broadcasting and 5G applications. The proposed antenna consists of a simple feeding network and an elliptical slot of appropriate ground plane dimensions. Further, this elliptical slot is rotated around its center, which will eventually produce CP operation in both frequency bands while maintaining the high isolation between the input ports. The generation of the perturbed cavity modes is also explained with the help of equivalent circuit analysis.

4.1.1 Antenna Design

4.1.1.1 SIW Cavity Design

The geometrical configuration of the proposed dual-polarized SIW cavity-backed slot antenna is shown in Fig. 4.1 where a low loss Rogers RT/Duroid 5880 copper lam-

inated dielectric substrate material of permittivity ε_r=2.2, loss tangent tanδ=0.0008 and thickness h=0.787 mm is used. The proposed antenna consists of a SIW cavity of dimension $L_{SIW} \times W_{SIW}$ as a resonator which is implemented using four rows of metallic vias of diameter d_{via}, separated by the distance p_{via} (or pitch) as depicted in Fig. 4.1(a).

The value of d_{via} and p_{via} is chosen in such a way that there will be minimum radiation loss and leakage of energy and given by [38]

$$\frac{p_{via}}{d_{via}} < 2 \tag{4.1a}$$

$$d_{via} < \frac{\lambda_g}{5} \tag{4.1b}$$

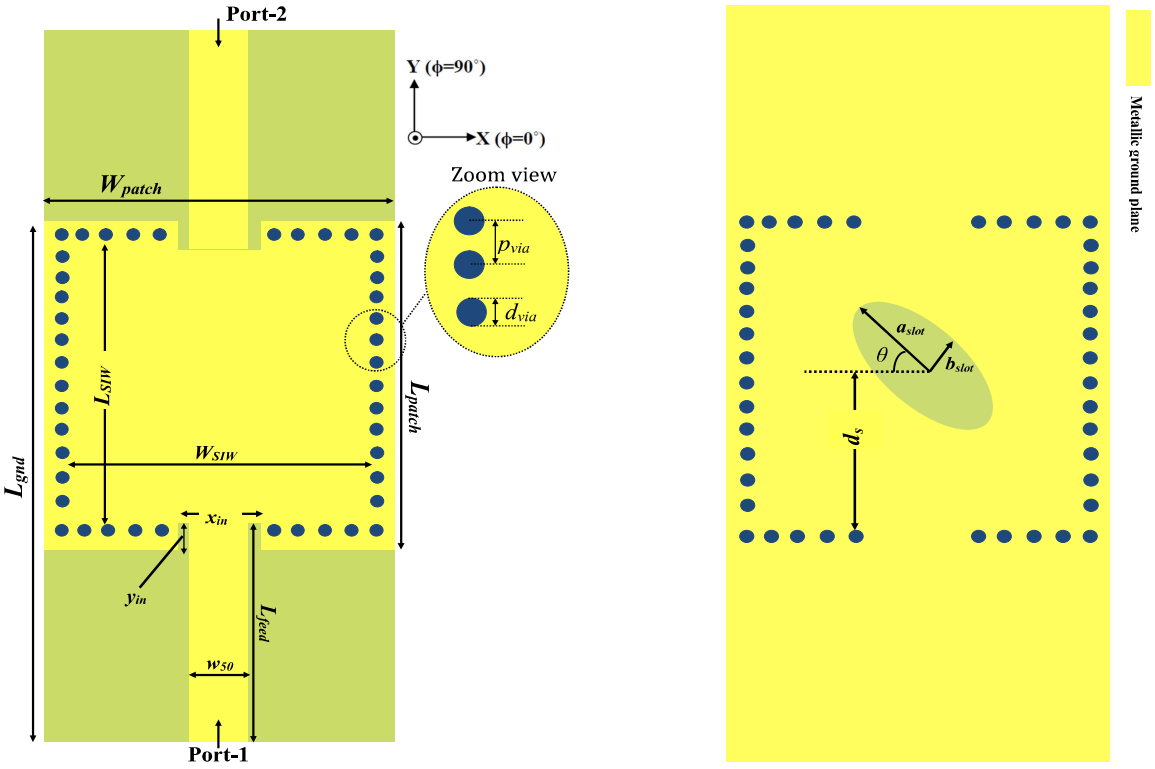

Figure 4.1: Schematic of the proposed antenna. (a) Top view (b) Bottom view. **Note:** W_{patch}=12, L_{patch}=12, L_{gnd}=19, W_{SIW}=10.40, L_{SIW}=10.40, w_{50}=2, L_{feed}=8, y_{in}=1, x_{in}=3.20, p_{via}=0.80, d_s=5 and d_{via}=0.40. All dimensions are in 'mm'.

The average value of the conductor losses (α_{ohmic}), dielectric losses (α_{diel}), radia-

tion losses (α_{rad}) are 2.87 dB, 1.70 dB, and 12 dB respectively within the range of operating frequency for port-1 and 4.61 dB, 2.50 dB and 18 dB respectively for port-2. The relationship between the resonance frequency for any TE_{mnp} of the SIW cavity formed by the metallic vias and geometrical parameters related to the proposed antenna dimensions can be calculated as follows [160]

$$f_r = \frac{c}{2\sqrt{\varepsilon_r}}\sqrt{(\frac{m}{W_{eff}})^2 + (\frac{n}{L_{eff}})^2 + (\frac{p}{h})^2} \tag{4.2a}$$

$$W_{eff}/L_{eff} = W_{SIW}/L_{SIW} - \frac{1.08p_{via}^2}{d_{via}} + \frac{0.1p_{via}^2}{W_{SIW}/L_{SIW}} \tag{4.2b}$$

where the terms m, n, p are the modal indices. The dimensions of the SIW cavity are chosen in such a way that they support and keep the dominant TE_{110} mode within the upper 5G band. Two separate microstrip lines having characteristic impedance of 50Ω are used for excitation and make the connections of 50Ω SMA connectors straightforward. An elliptical slot is etched in the metallic ground plane at an offset distance of d_s ($\neq \frac{L_{SIW}}{2}$) from the center as shown in Fig. 4.1(b). The asymmetric position of the elliptical slot divides the whole SIW cavity into two unequal parts. This will generate two different resonant modes due to perturbed electric field ($\vec{\boldsymbol{E}}$) when excited separately with port-1 and 2 as shown in Fig. 4.2(a). The frequency bands generated are centered around 21.50 GHz (21.37-21.64 GHz; 1.26%) and 28.05 GHz (27.42-28.63 GHz; 4.32%). The surface current distribution at 21.50 GHz and 28.05 GHz frequency bands is shown in Fig. 4.2(b) and 4.2(c), respectively. Fig. 4.2(b) shows the surface current which is mainly concentrated in the upper-half of the SIW cavity while excited with port-1 only. Similarly, when port-2 is excited, the current density mainly concentrates only around lower-half of the SIW cavity. The electric field generated around the elliptical slot when excited either with port-1 or port-2 are out-of-phase with each other and hence, helps the proposed SIW cavity antenna to radiate into the free space as a dual-port dual-band antenna. The longitudinal placement of elliptical slot prevents the spilling

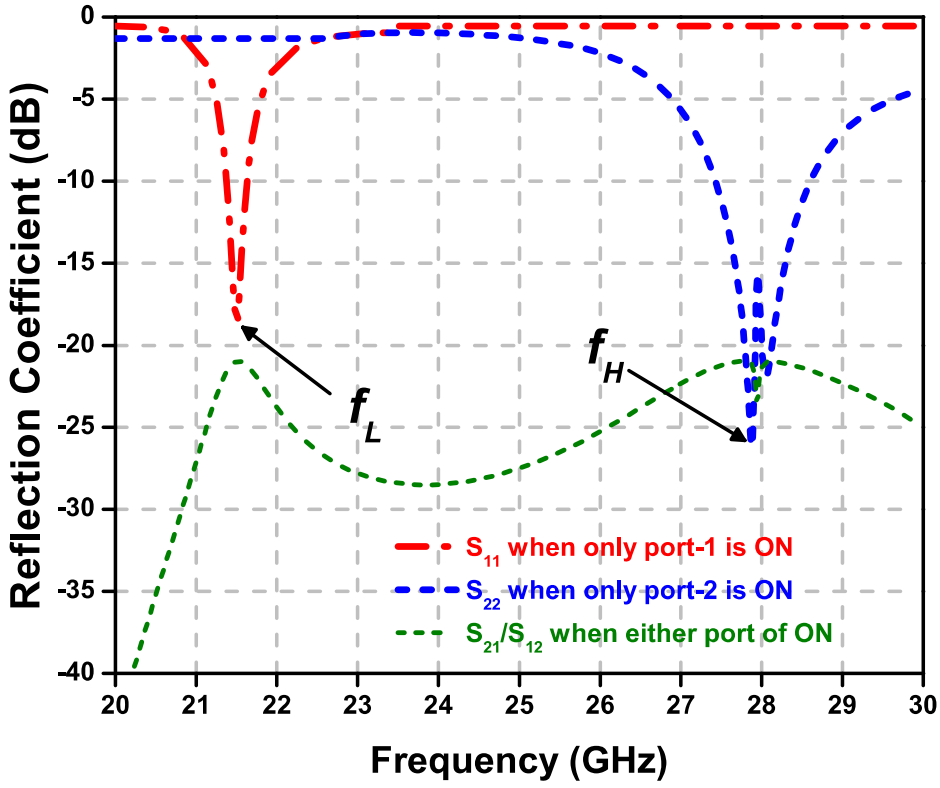

(a)

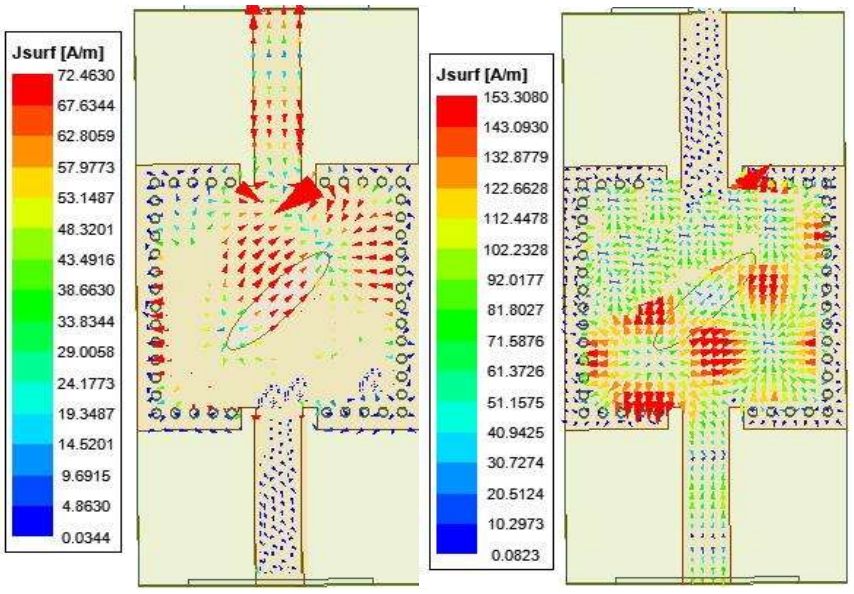

(b) (c)

Figure 4.2: (a) S_{11} of the proposed antenna when excited separately with each port; Surface current density at (b) 21.50 GHz and (c) 28.05 GHz, when excited only with port-1 and port-2, respectively.
Note: f_L(=21.50 GHz) and f_H(=28.05 GHz) are the operating frequency bands generated when excited either with port-1 or port-2, respectively.

of electromagnetic waves from one port to other. The negligible transmission (S_{12}/S_{21}) from one port to other as depicted from Fig. 4.2(a) [green dotted line] enhances the isolation between them.

4.1.1.2 Effect of elliptical slot

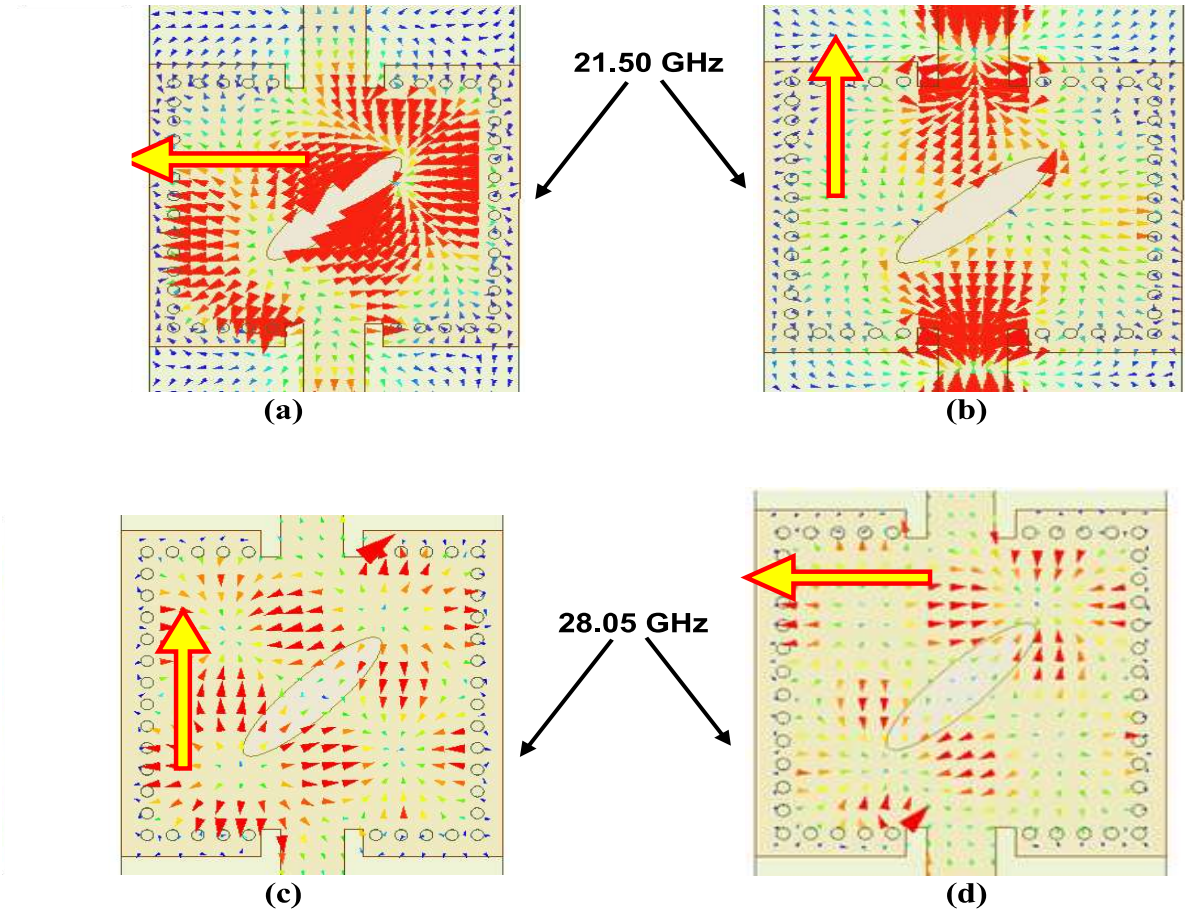

Figure 4.3: Plots of vector surface current density (a) ωt=0°, (b) ωt=90° taken at 21.50 GHz and (c) ωt=0°, (b) ωt=90° taken at 28.05 GHz when excited from port-1 and port-2, respectively.

A rotated elliptical slot having semi-major axis a_{slot} and rotation angle θ is etched in the ground plane as shown in Fig. 4.1(b) due to which the SIW cavity is segmented into two unequal resonators. The dual-frequency ($f_{11}^{even,odd}$) corresponding to dominant $TM_{11}^{even,odd}$ mode of an elliptical slot of given eccentricity and semi-major axis is given

by [157]:

$$(f_{11}^{even,odd}) = \frac{15}{\pi e_{slot} a_{slot}} \sqrt{\frac{q_{11}^{even,odd}}{\varepsilon_r}} \tag{4.3}$$

where $e_{slot}(=\sqrt{1-(\frac{b_{slot}}{a_{slot}})^2})$ is the eccentricity of the elliptical slot, b_{slot} is the semi-minor axis length, $q_{11}^{e,o}$ is an approximated Mathieu function which can be calculated as follows [161]:

$$q_{11}^{even} = -0.0049e_{slot} + 3.7888e_{slot}^2 - 0.7228e_{slot}^3 + 2.2314e_{slot}^4 \tag{4.4a}$$

$$q_{11}^{odd} = -0.0063e_{slot} + 3.8316e_{slot}^2 - 1.1351e_{slot}^3 + 5.2229e_{slot}^4 \tag{4.4b}$$

The elliptical slot present in the metallic ground plane is rotated around its center (having rotation angle θ as shown in Fig. 4.1(b)) that generates two orthogonal $\overrightarrow{\boldsymbol{E}}$-field vectors of almost equal amplitude and phase difference of 90° and hence CP operation is obtained. The variation in distance d_s and rotation angle θ helps in achieving wide axial-ratio bandwidth (ARBW) in both lower and upper frequency bands. Fig. 4.3 shows the vector surface current distribution ($\overrightarrow{\boldsymbol{J}}$) at 21.50 GHz and 28.05 GHz when excited from port-1 and port-2, respectively. It is evident that the proposed antenna shows RHCP behavior (clockwise movement of $\overrightarrow{\boldsymbol{J}}$) when excited with port-1 and LHCP when excited with port-2 (anticlockwise movement of $\overrightarrow{\boldsymbol{J}}$).

Furthermore, the purity of LHCP/RHCP behavior can also be confirmed from polarization conversion ratio (PCR), which can be defined as where $r_{xy} = |\vec{E}_x^r/\vec{E}_y^i|$ and $r_{yy} = |\vec{E}_y^r/\vec{E}_y^i|$ represent the ratio of E-field in y-to-x and y-to-y polarization conversion, respectively [162]. The magnitude of RHCP is remarkably higher than LHCP magnitude in lower frequency band and that of LHCP than RHCP in upper frequency band as shown in Fig. 4.4.

$$PCR = r_{xy}^2 / \left(r_{xy}^2 + r_{yy}^2\right) \tag{4.5}$$

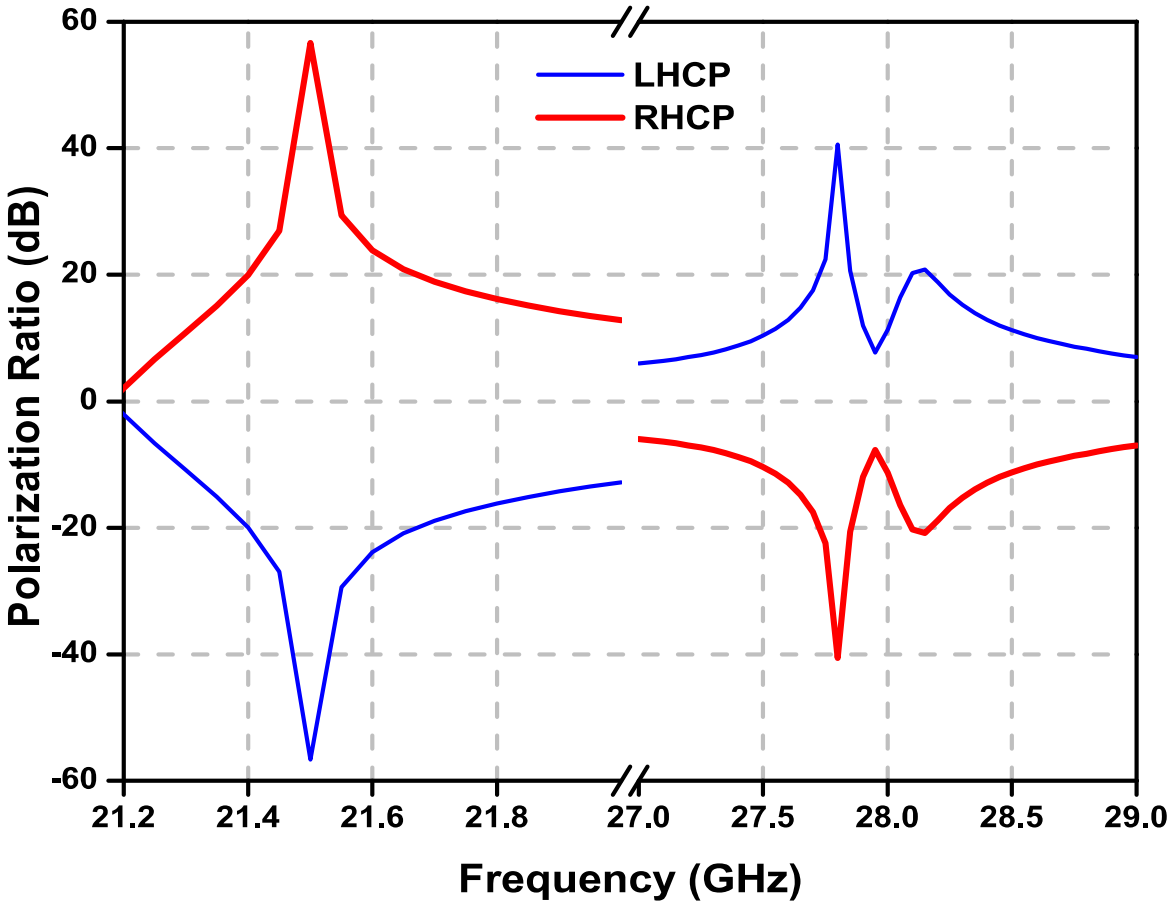

Figure 4.4: Polarization conversion ratio (PCR) for the proposed SIW antenna.

4.1.2 Equivalent Circuit Model

To understand the propagating modes within the SIW cavity, the proposed antenna is analyzed with the help of equivalent circuit model. A Keysight Advanced Design System (ADS) software is used to simulate and optimize the equivalent circuit of the proposed SIW cavity antenna. The SIW cavity can be modeled as a parallel combination of LCR resonant circuit corresponding to each propagating resonating mode [163]. Therefore, the frequency bands generated around 21 GHz and 28 GHz can be modeled as three parallel LCR circuits where n_a, L_{CL}, C_{CL} and R_{CL} corresponds to lower 21.50 GHz resonant mode while n_H, L_{CH}, C_{CH} and R_{CH} corresponds to higher 28.05 GHz frequency bands as shown in Fig. 4.5.

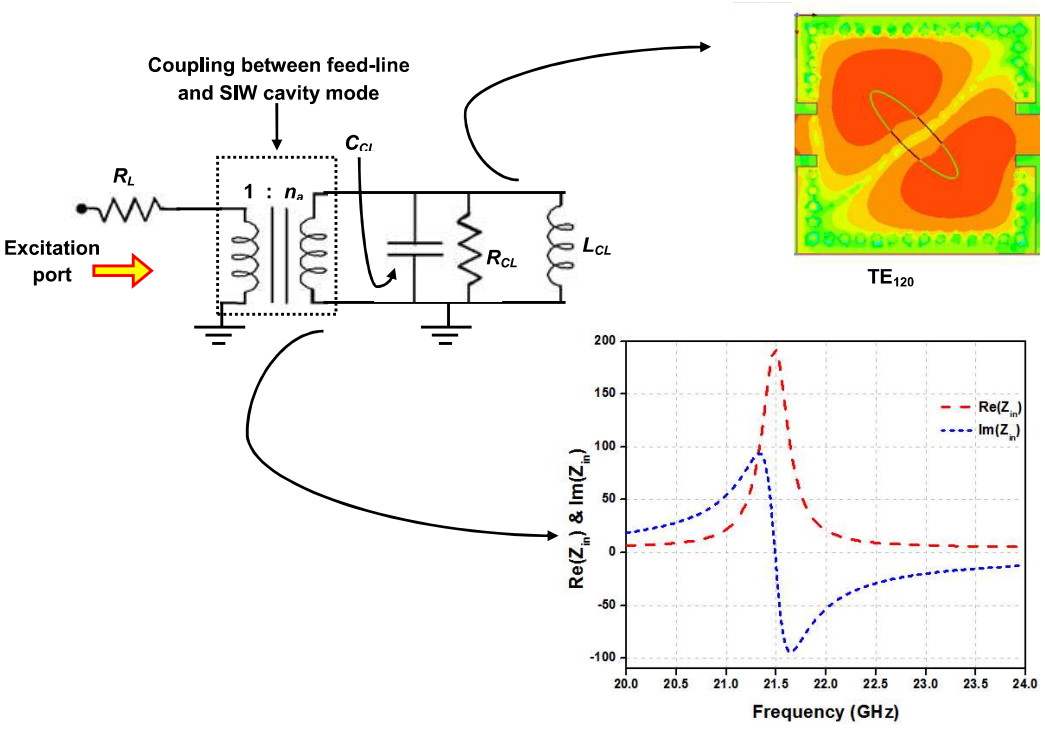

(a)

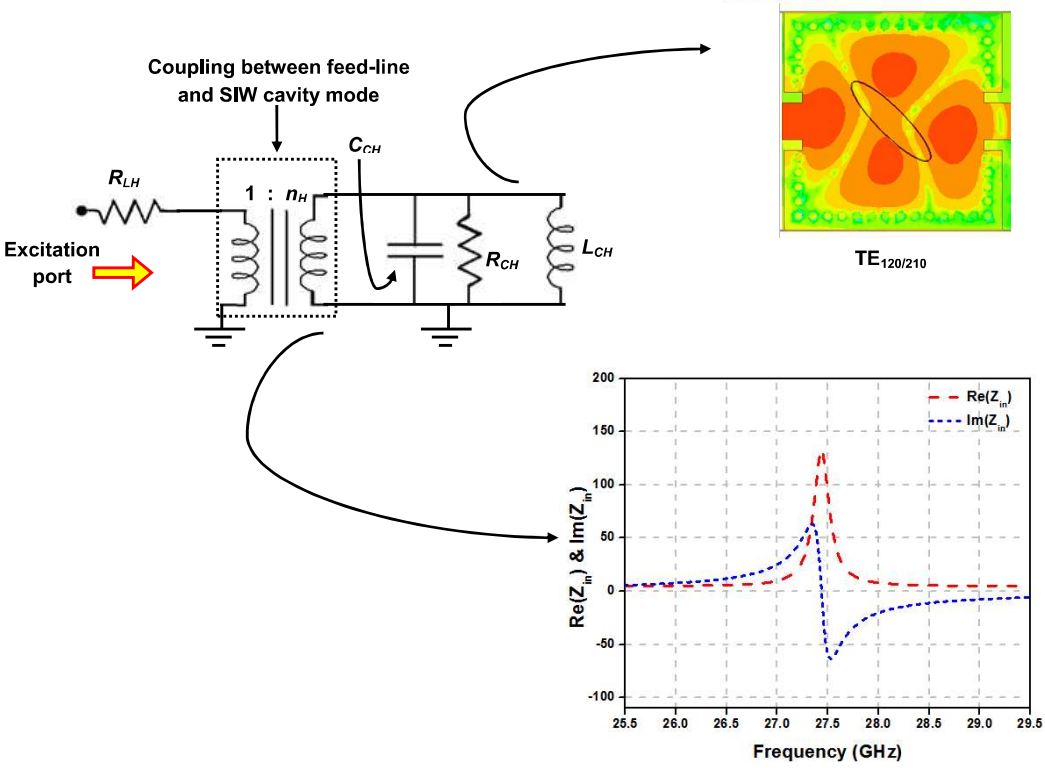

(b)

Figure 4.5: Equivalent circuit model of the proposed antenna for (a) lower and (b) higher resonant mode.
Note: The modal parameters are: n_a=18.29, C_{CL}=8.08fF, R_{CL}=63 KΩ, L_{CL}=6.79 nH, n_H=25, C_{CL}=11fF, R_{CL}=80.26 KΩ, L_{CL}=3.05 nH and R_L=4.68 Ω

4.1.3 Parametric Study

As discussed in previous sections, the resonating frequencies obtained depend mainly on cavity and slot dimensions. Also, slot position can also be changed to tune the lower and upper frequencies (or f_H/f_L) and to obtain high level of isolation between the input ports. Here, the effect of distance d_S, rotation angle θ and slot dimensions in terms of eccentricity e on antenna matching characteristics is discussed.

4.1.3.1 Effect of distance d_s:

Both lower and upper resonant frequencies of the proposed antenna varies with the change in the position of the slot position d_s as shown in Fig. 4.6(a). It is observed that the lower resonant frequency decreases from 22.06 GHz to 21.50 GHz while upper resonant frequency increases from 27.87 GHz to 28.50 GHz with increase in distance d_s from 3 mm to 6 mm. Correspondingly, the frequency ratio ($=\frac{f_H}{f_L}$) varies from 1.26 to 1.33 while maintaining a good level of isolation (or S_{21} $\geq$22 dB) between the input ports.

4.1.3.2 Effect of rotation angle, θ of elliptical slot:

The elliptical slot is rotated around its center in order to bring the CP operation in the desired frequency bands. The effect of rotation angle θ on matching characteristics is shown in Fig. 4.6(b). It is evident that as θ goes from 0° to 60°, the lower and upper resonating frequencies shifts from 20.95 to 21.05 GHz and 27.10 GHz to 28.35 GHz, respectively. The percentage bandwidth in lower and upper frequency bands shifts from 0% to 1.39% and 0.37% to 4.28% as θ varies from 0° to 45°. At θ=60°, the upper band splits into two separate frequency bands, centered around 27.40 GHz and 28.35 GHz whereas lower frequency bands shifts to 21.05 GHz. The another effect of rotation angle θ on axial ratio is illustrated in Fig. 4.7(a). At θ=0°, no CP operation is seen in both upper and lower frequency bands. As θ approaches to 15°, CP in only upper resonating

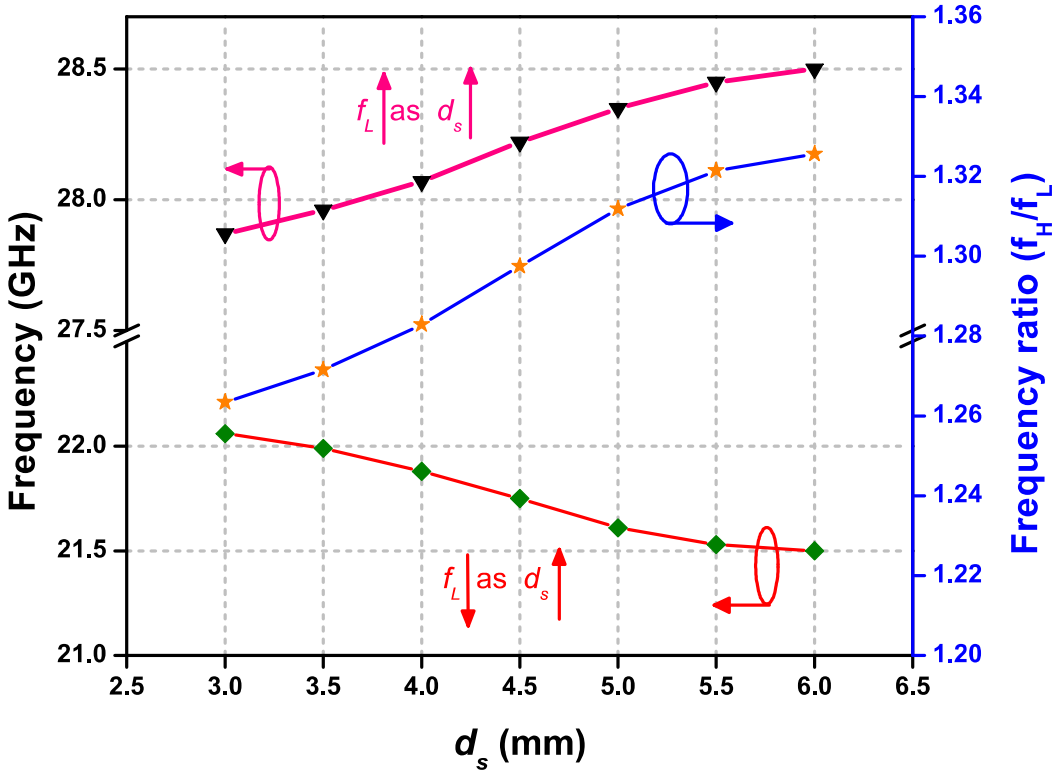

(a)

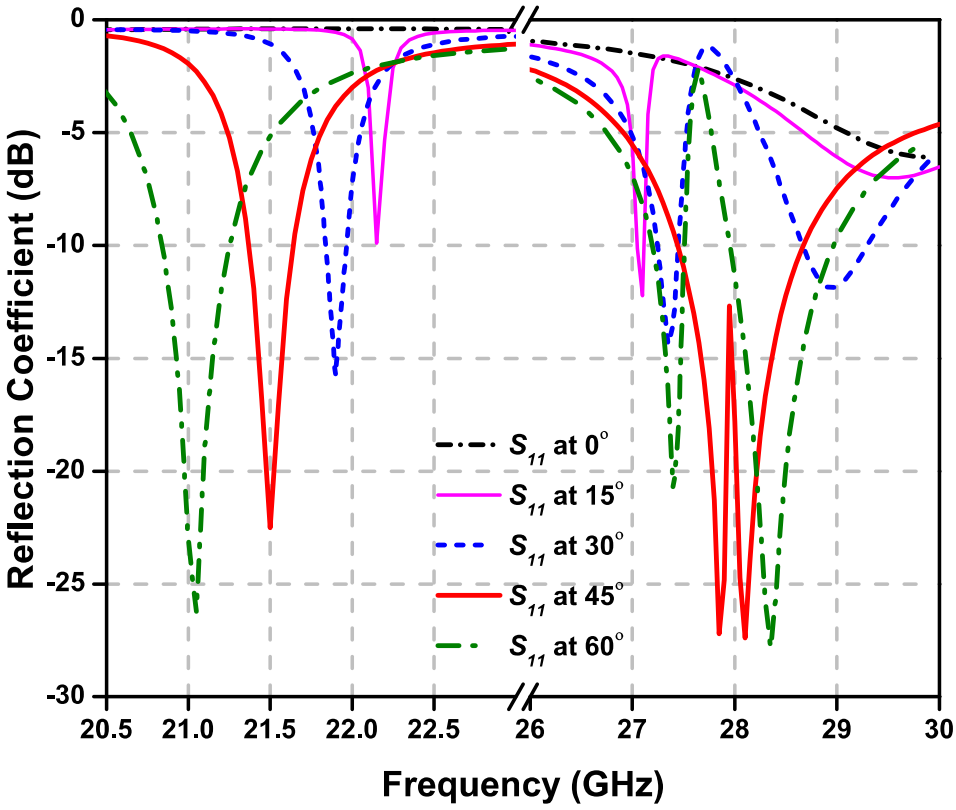

(b)

Figure 4.6: Effect of (a) distance d_s, and (b) rotation angle θ with S_{11}.

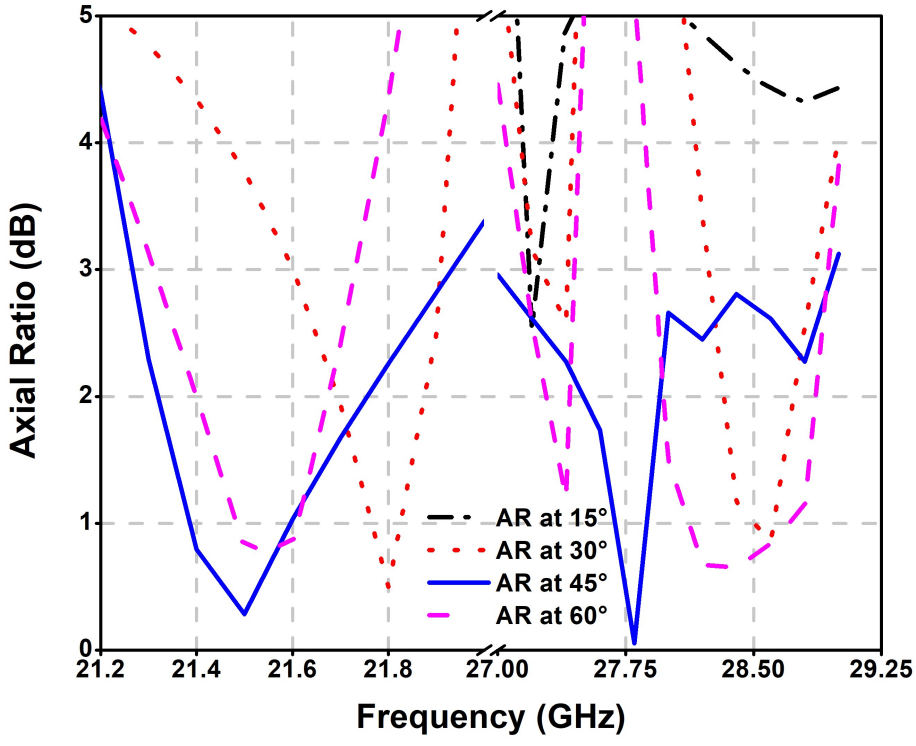

(a)

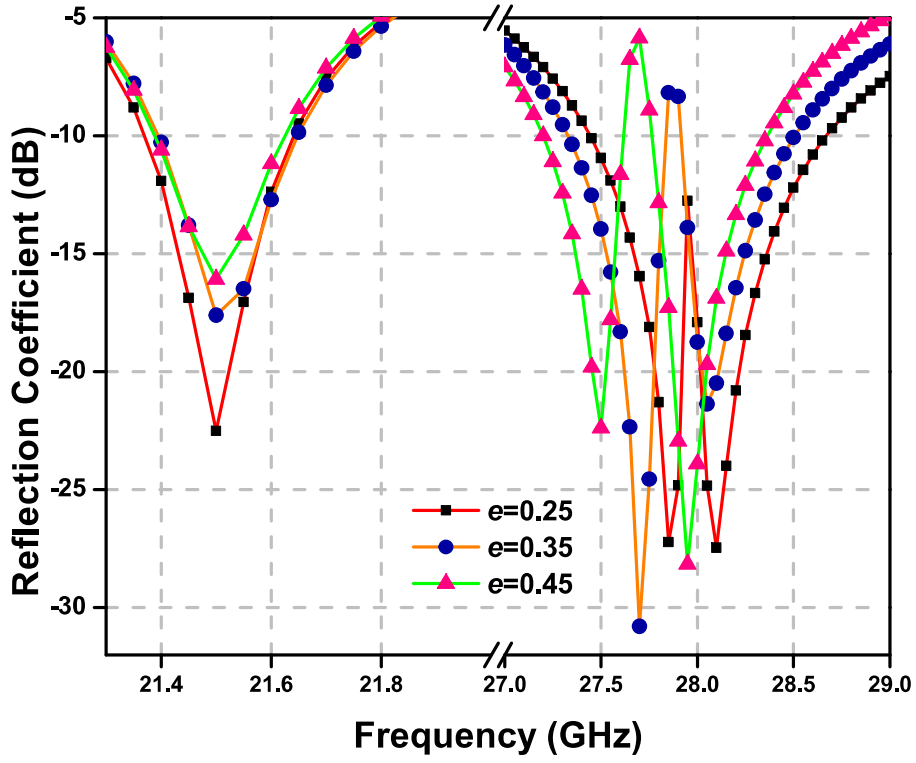

(b)

Figure 4.7: Effect of (a) rotation angle θ with AR, and (b) eccentricity of elliptical slot on matching characteristics.

frequency (around 27.2 GHz) is seen as depicted from Fig. 4.7(c). For further increase in θ, the maximum ARBW of 3.01% and 6.62% for lower and upper frequency bands, respectively is reported at θ=45°. As θ reaches to 60°, the ARBW goes down to 2.73% and no CP operation is seen beyond 60°.

4.1.3.3 Effect of eccentricity, *e* of elliptical slot:

The effect of eccentricity e of the elliptical slot on matching characteristics is shown in Fig. 4.7(b). It is observed that the effect of e is negligible on lower frequency band whereas the upper frequency band divides into two as e goes from 0.25 to 0.45 (or becomes more like a circle).

4.1.4 Experimental Results and Discussion

4.1.4.1 Matching Characteristics:

The photograph of the fabricated prototype (front side, back side and having the SMA connectors while testing) of the proposed SIW cavity antenna is shown in Fig. 4.8(a). The Keysight N9951A FieldFox Microwave Analyzer is used to measure all S-parameters of the proposed antenna. The comparison of the simulated and measured S-parameters of the proposed antenna is illustrated in Fig. 4.8(b). The measured results show that the proposed antenna supports two different frequency bands, i.e., within 21.38-21.92 GHz (2.49%) and 26.68-27.58 GHz (3.32%) frequency bands, S_{11} is below -10 dB.

4.1.4.2 Gain, Efficiency and Radiation Pattern Characteristics:

The measurements related to gain, efficiency and radiation pattern are performed inside the properly calibrated anechoic chamber where a horn antenna of known gain is placed at a distance of 8.1 metres away from the proposed antenna (whose gain/radiation pattern has to be measured). The measurement setup for the same is shown in Fig. 4.9(a).

The peak gain and efficiency are measured for the given operating frequency band

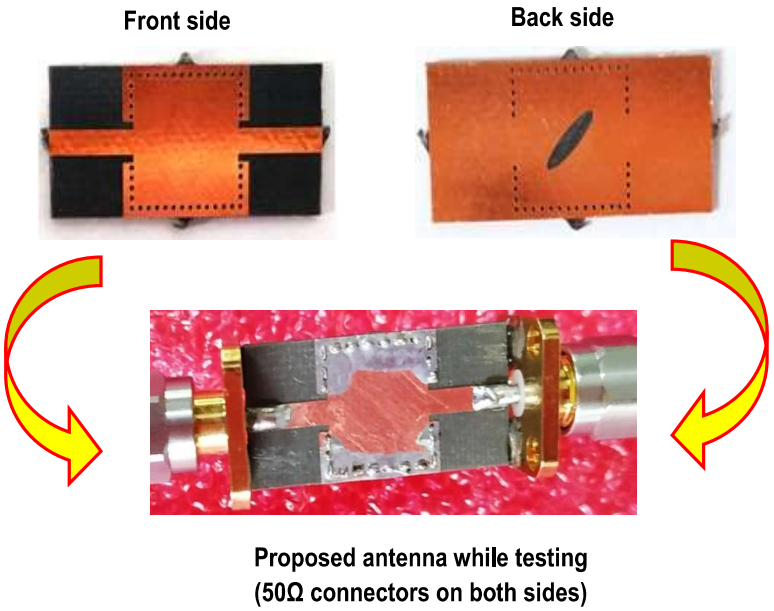

(a)

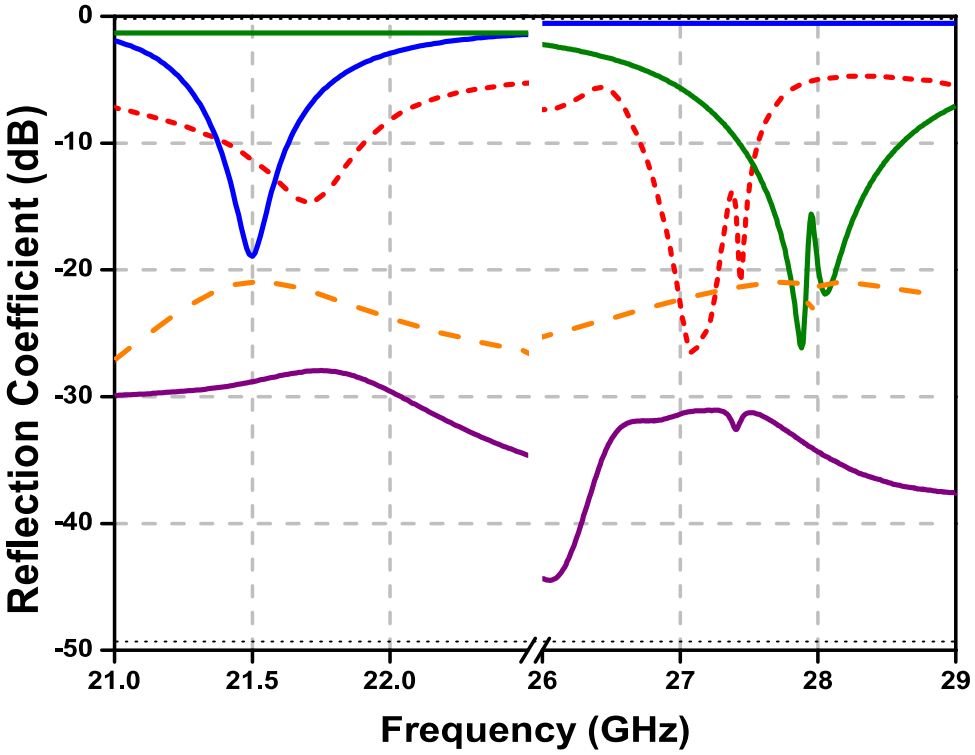

(b)

Figure 4.8: (a) Fabricated version of the proposed SIW antenna and (b) simulated S_{11}, S_{22} and S_{12}/S_{21} of the proposed SIW antenna.
Note: (i) Solid blue line: simulated S_{11} when only port-1 is ON; (ii) solid green line: simulated S_{11} when only port-2 is ON; (iii) solid violet line: simulated S_{12}/S_{21}; (iv) orange dotted line: measured S_{12}/S_{21}; (v) red dotted line: measured S_{11} when either port is ON.

against frequency at θ=ϕ=0° as shown in Fig. 4.9(b). The peak gain varies from 5.69 to 7.70 dBic with an average gain of 6.69 dBic within the lower operating frequency band. Also, the peak gain varies from 7.88 to 9.84 dBic with an average gain of 8.77 dBic within the upper operating frequency range. Fig. 4.9(b) also shows the radiation efficiency of the proposed wide-slot antenna. It is seen that the radiation efficiency at θ=ϕ=0° varies from 70.37% to 97.49% and 82.16% to 95.19% within the lower and upper operating frequency range, respectively. The average radiation efficiency within lower and upper operating frequency range is 82.95% and 87.62%, respectively.

The radiation patterns of the proposed antenna in *YZ*-plane (ϕ=0°) and *XZ*-plane (ϕ=90°) at 21.70 GHz and 27.10 GHz (resonating frequencies of lower and upper frequency bands) are plotted in Fig. 4.10. It is evident from Fig. 4.10 that measured results are in good agreement with corresponding simulated patterns. A small inconsistency in both the results due to fabrication tolerance may be attributed. Tolerances for simulated vs. experimental resonating frequencies of the proposed antenna are ±0.73% for port-1 and ±1.2% port-2. It is also observed that an isolation of >22 dB in both frequency bands is obtained. The measured cross-polarization is about (38, 40 dB) in *YZ*-plane and (31, 38 dB) in *XZ*-plane at the frequencies 21.70 GHz and 27.10 GHz, respectively. The front-to-back ratio (FTBR) in all cases is better than 15 dB.

4.1.4.3 Axial-Ratio versus Frequency

The measured 3-dB ARBW for both the frequency bands of the proposed SIW cavity antenna is about 650 MHz (21.25-21.90 GHz) and 1850 MHz (27-28.85 GHz) at θ=ϕ=0° is shown in Fig. 4.11. The measured percentage ARBW for both frequency bands is 3.01% and 6.62% which lies slightly out of the measured operating frequency range. The minimum axial ratio of 0.02 dB and 0.52 dB at 21.5 GHz and 27.80 GHz, respectively is obtained.

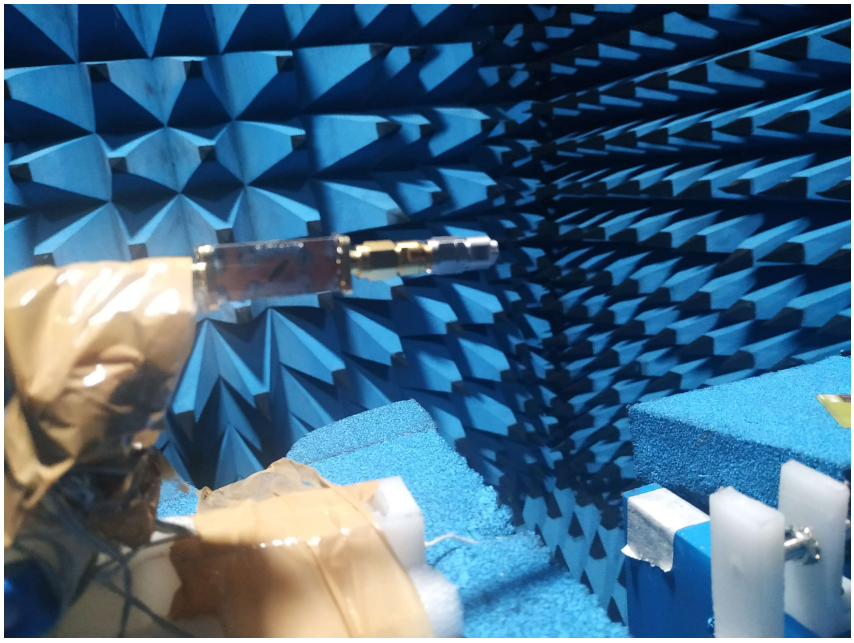

(a)

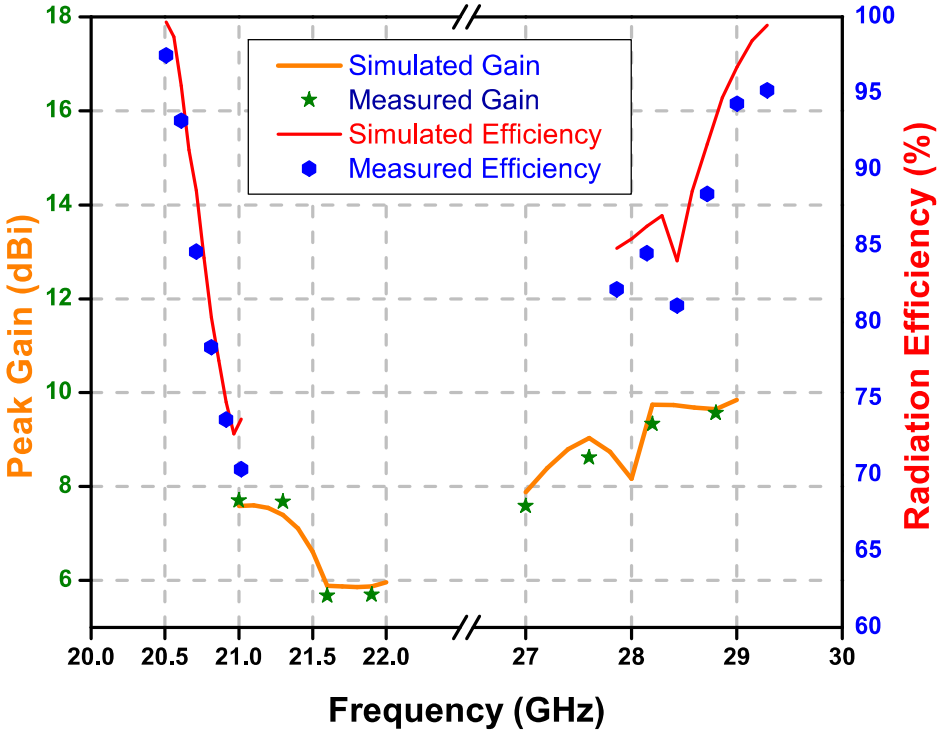

(b)

Figure 4.9: (a) Proposed SIW cavity-backed antenna inside anechoic chamber during gain/efficiency and radiation pattern measurement; simulated/measured and (b) gain/radiation efficiency.

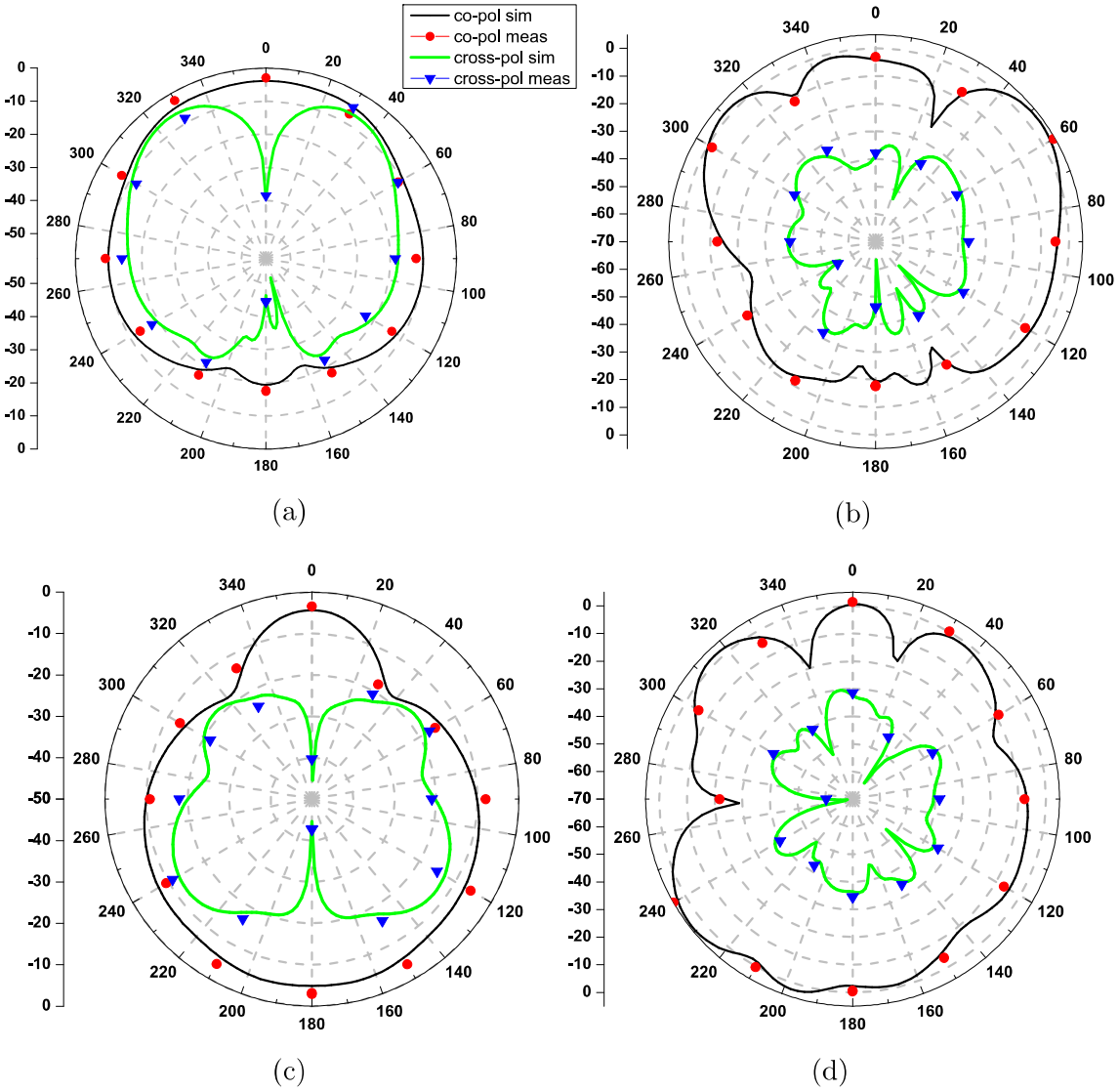

Figure 4.10: Simulated and measured radiation patterns
(a) ϕ=0°, (b) ϕ=90° at 21.70 GHz when excited with port-1 only; (c) ϕ=0°, (d) ϕ=90° at 27.10 GHz when excited with port-2 only.

Table 4.1: Comparison with other SIW based diplexers present in the literature

LP/CP Antenna	Parameters		[164]		[18]		[165]		[166]		[167]		[168]		[169]		[170]
	Excitation port		Port-1	Port-2	Port-1	Port-2	Port-1	Port-2	Port-1	Port-2	Port-1	Port-2	Port-1	Port-2	Port-1	Port-2	Port-1	Port-2
LP	10 dB IBW	GHz	4.26–4.31	7.47–7.60	NR		3.9–4.37	4.69–5.34	8.22–8.36	10.32–10.6	NR		5.11–5.23	5.75– 5.89	NR	8.47–8.63	0.71–0.83	
		%	1.16	1.72	NR		11.30	14.24	1.93	2.68	1.32	1.46	2.32	2.40	NR	1.04	0.91	
	Isolation (dB)		>40.5	>32.2	25		NR		29.2	30.2	29		33.2	33.8	22.2	25.7	20	18
	Gain (dBi)		5.38	5.82	4.3	4.2	3.82	4.48	3.56	5.24	5.75	5.95	3.31	4.16	4.0	4.3	5.7	5.9
	Size (mm^2)[1]		NR		NR		38×38		32×26		NR		NR		NR		NR	
	Radiation Efficiency (%)		95.1	95.1	NR		65	64	NR		NR		60	70	NR		NR	
	Parameters		[82]	[83]	[84]	[85]	[86]	[87]	[88]	[89]	This work							
CP	10 dB IBW	GHz	37.25–37.25	27.25–28.53	5.8	12.69–12.6	5.65–5.78	34.67–35.15	11.87–12.19	12.15–12.38	11.48–11.91	21.38–21.92	26.68–27.58					
		%	1.1	6.3	2.4/2.6	4.2	1.16	1.5	2.7	1.87	3.67	2.49	3.32					
	3 dB ARBW	GHz	37–37.4	27.85–28.25	NR	-	5.7–5.72	34.52–35.38	12-12.11	12.27–12.37	11.67–11.86	21.25–21.9	27–28.85					
		%	1.1	1.8	0.9	1.6	0.35	2.4	0.9	0.81	1.61	3.01	6.62					
	Isolation (dB)		NR		NR	NR	NR	NR	NR	18.52	14.05	>22	>22					
	Gain (dBic)		5	5.9	6.57/6.98	7.4	7.06	18.14	8.49	5.6	5.9	6.69	8.77					
	Size (mm^2)		NR	37×37	NR	NR	NR	NR	16.2×16.2		NR		26×12					
	Radiation Efficiency (%)		88	NR	86.8/87	NR	NR	NR	NR		NR		82.95	87.62				
	Polarization State:		LHCP	RHCP	RHCP	LHCP	RHCP	RHCP	RHCP/LHCP	RHCP	LHCP	RHCP	LHCP					
	Technique Used:		Two annular slots	Spoon-shaped slot	Chamfered cornered patch	Multiple elliptical slots	Arc-shaped slot	Rotated Koch slot	Rectangular slots	Asymmetric cross-slot		Elliptical slot						

NR: Not reported

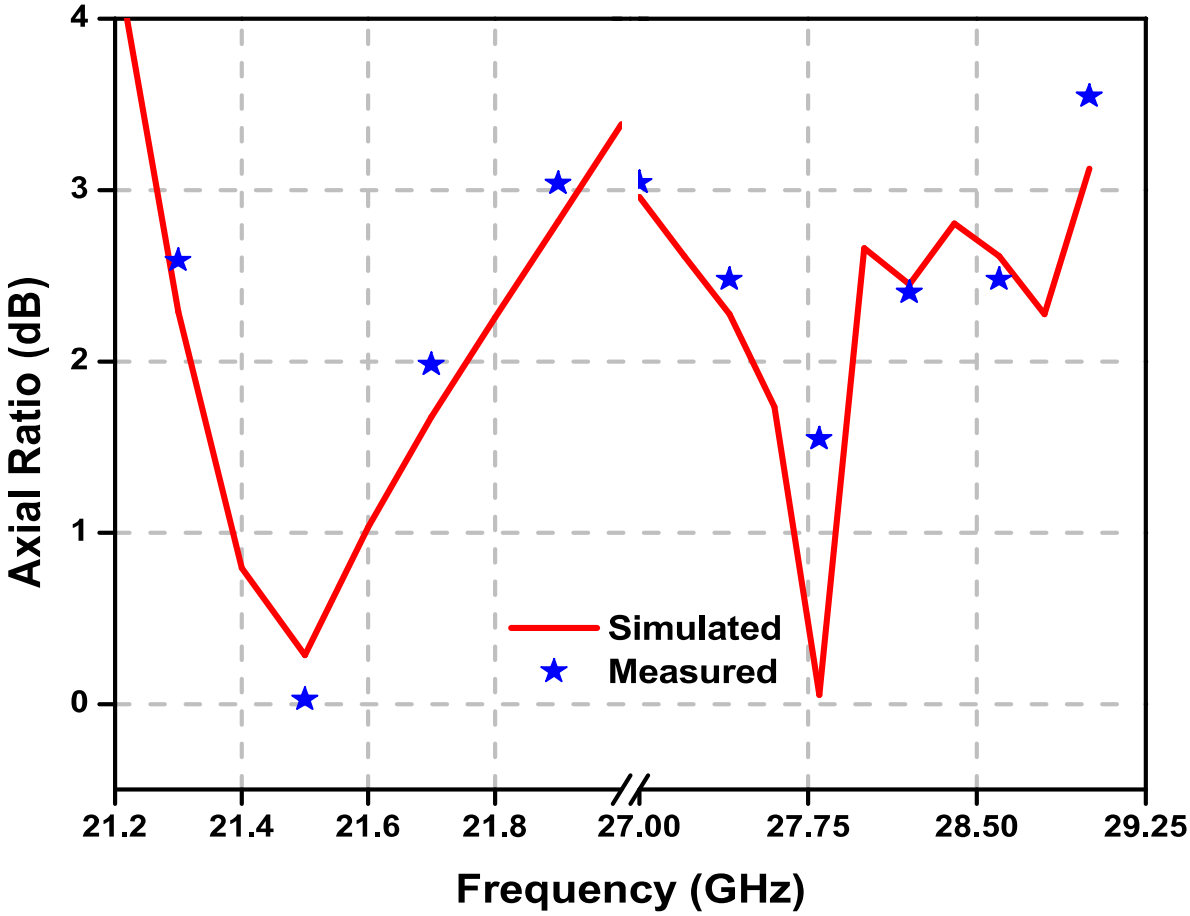

Figure 4.11: Simulated versus measured axial-ratio of the proposed antenna.

4.1.5 Comparison Analysis

Table 1 shows the comparison of the proposed dual-band dual-sense CP SIW antenna with other reported SIW based diplexers and CP antenna structures. The main contributions of the proposed work along with its comparison with existing antenna structures as discussed in this chapter are as follows:

(I) **Linearly polarized SIW diplexers:**

(i) **Comparison in terms of size:** The proposed antenna possesses more compact physical dimensions as compared to antenna structures reported in [18, 164–170]. This is achieved due to the perturbation of dominant TE_{110} and hybrid mode generated due to merging of TE_{130} and TE_{310} modes. These

degenerated modes arise due to loading of elliptical slot on the SIW cavity.

(ii) **Comparison in terms of impedance bandwidth:** The proposed antenna has highest 10 dB impedance bandwidth (IBW) among SIW based diplexers reported in [18,164–170] except [165]. However, the peak gain and maximum radiation efficiency of the proposed antenna is about 4.29 dB and 33.49%, respectively better than the antenna structure reported in [165].

(iii) **Overall advantage:** The proposed antenna exhibits self-diplexing mechanism along with flexibility in tuning frequency ratio from 1.26-1.33, compact size, high gain, high isolation of more than 22 dB and front-to-back ratio (FTBR) of more than 15 dB in both frequency bands.

(II) **Circularly polarized SIW antennas:**

(i) The proposed antenna shows simple geometry, high 10 dB IBW, compact size among the SIW based antenna structures reported in [82–89].

(ii) The 3 dB ARBW of the proposed antenna is also highest among the antennas discussed in [82–89].

(iii) The proposed antenna shows both LHCP and RHCP polarization states whereas the antenna structures reported in [82–87] either show LHCP or RHCP polarization state.

(iv) **Overall advantage:** The proposed antenna is best suited for 5G applications including 26.50-27.50 GHz in Italy and Switzerland, 26 GHz in Germany and France, 24.25-27.50 GHz in India. In 21.38-21.90 GHz in amateur satellite, broadcasting, and Amateur radio operators which includes terrestrial, satellites and planetary communications.

4.2 On the behaviour of Self-Triplexing SIW Cavity Backed Antenna with Non-Linear Replicated Hybrid Slot for C and X-band Applications

Here, a compact SIW based STA with two orthogonally placed microstrip feed lines and one coaxial probe is presented. The proposed design consists of a single large SIW cavity designed over a single substrate layer with a hybrid slot which is a combination of a hexagonal slot and two narrow rectangular slots. After applying scaling non-linear replications (NLR) over the hexagonal slot in both vertical and horizontal directions, the self-diplexing operation with two resonances around 5.23 and 7.50 GHz is reported. For self-triplexing operation, the space inside the hexagonal slot is filled with similar parasitic hexagonal patch and fed by coaxial probe. This generates resonance around 10.82 GHz which can be modelled using the gap between the parasitic patch and hexagonal slot. The independent tuning of each frequency band, isolation and radiation characteristics are also discussed in detail. Finally, the proposed STA is fabricated using standard PCB process and good agreement between the experimental and simulated results is found. The main contributions of the proposed SIW based STA are:

1. To the author's best knowledge, the proposed SIW-based STA is the first of its kind in the literature where the concept of NLR is utilized for obtaining self-triplexed operation.
2. Easy independent tuning of all the three frequency bands is allowed using scaling of the hexagonal slot in x- and y-directions and spacing (or gap) between the hexagonal parasitic patch and hexagonal slot. Hence, the flexible operation of the proposed STA can be easily utilized for different frequency bands in C-, and X-band.
3. The proposed STA is highly compact as compared to already proposed SIW based

STAs in the literature [100]- [101] which added merit to the proposed design.

4. The orthogonal placement of the feed lines results into the weak coupling between the excitation ports, i.e., better than 43 dB. Therefore, the proposed antenna possesses the highest isolation as compared to existing STAs discussed in [100]-[101].

4.2.1 Proposed Antenna Design and Analysis

Fig. 4.12 illustrates the proposed SIW-based cavity-backed STA with finely tuned dimensions. The proposed STA design consists of a square SIW-cavity ($W_{CAV}\times L_{CAV}$), a regular hexagonal slot (side length, S_{out}) merged with two rectangular slots (slot-1: $w_{slot}\times L_{arm1}$, slot-2: $w_{slot}\times L_{arm2}$) and orthogonally placed feed lines, each having dimensions of $L_{feed}\times w_{feed}$. The proposed STA uses a 0.787 mm thick RT/Duroid-5880 with a dielectric constant ε_r=2.2 and a dielectric loss tangent tanδ=0.0002.

4.2.1.1 Cavity design

The SIW cavity is implemented by scooping out the cylindrical vias of diameter d_V and pitch p_V from the substrate material used and filled them with the copper. Four rows of such metal filled vias around the metallic patch make four sidewalls of the SIW cavity. The value of parameters d_V and p_V are chosen maintaining the condition $\frac{d_V}{\lambda_0} \leq 0.1$ and $\frac{d_V}{p_V} \geq 0.5$ (where λ_o is the free space wavelength) so as to ensure the negligible power leakage through the SIW cavity sidewalls [29]. The relationship between the resonating frequency of the SIW cavity with its dimensions is given as follows: [171]

$$f_{mnp} = \frac{1}{2\sqrt{\varepsilon\mu}}\sqrt{(\frac{m}{W_{cav,eff}})^2 + (\frac{n}{L_{cav,eff}})^2 + (\frac{p}{c})^2} \tag{4.6a}$$

where

$$L_{cav,eff} = L_{cav} - 1.08\frac{d_V^2}{p_V} + 0.1\frac{d_V^2}{L_{cav}} \tag{4.6b}$$

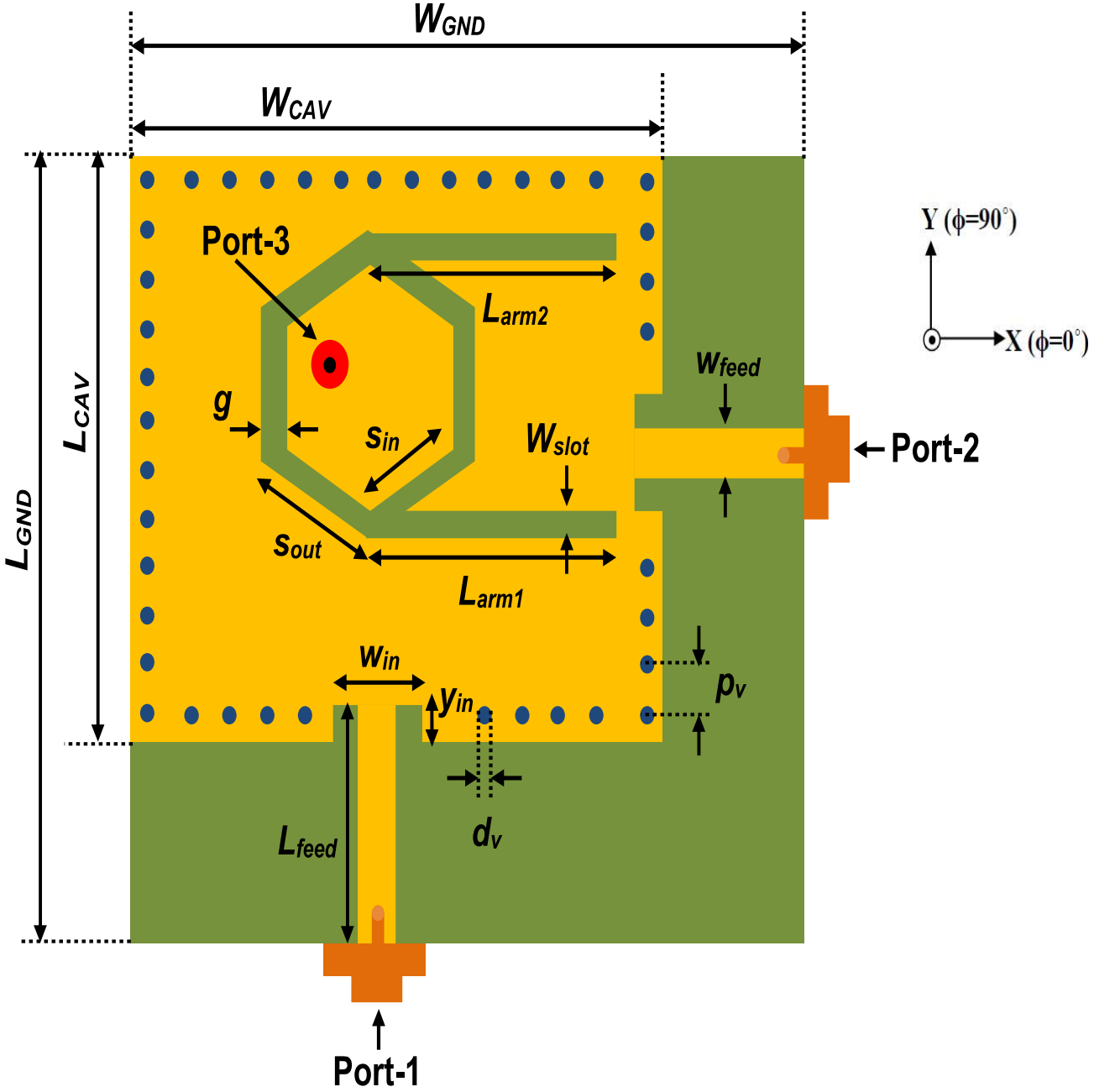

Figure 4.12: Schematic of the proposed antenna. The modal parameters are: W_{GND}=29, L_{GND}=29, W_{CAV}=24, L_{CAV}=24, L_{arm1}=9.5, L_{arm2}=9.5, w_{slot}=1.5, S_{in}=5.5, S_{out}=6, g=0.5, w_{feed}=2, L_{feed}=7.4, w_{in}=2.4, y_{in}=2.4, p_V=2 and d_V=1 (Units: mm).

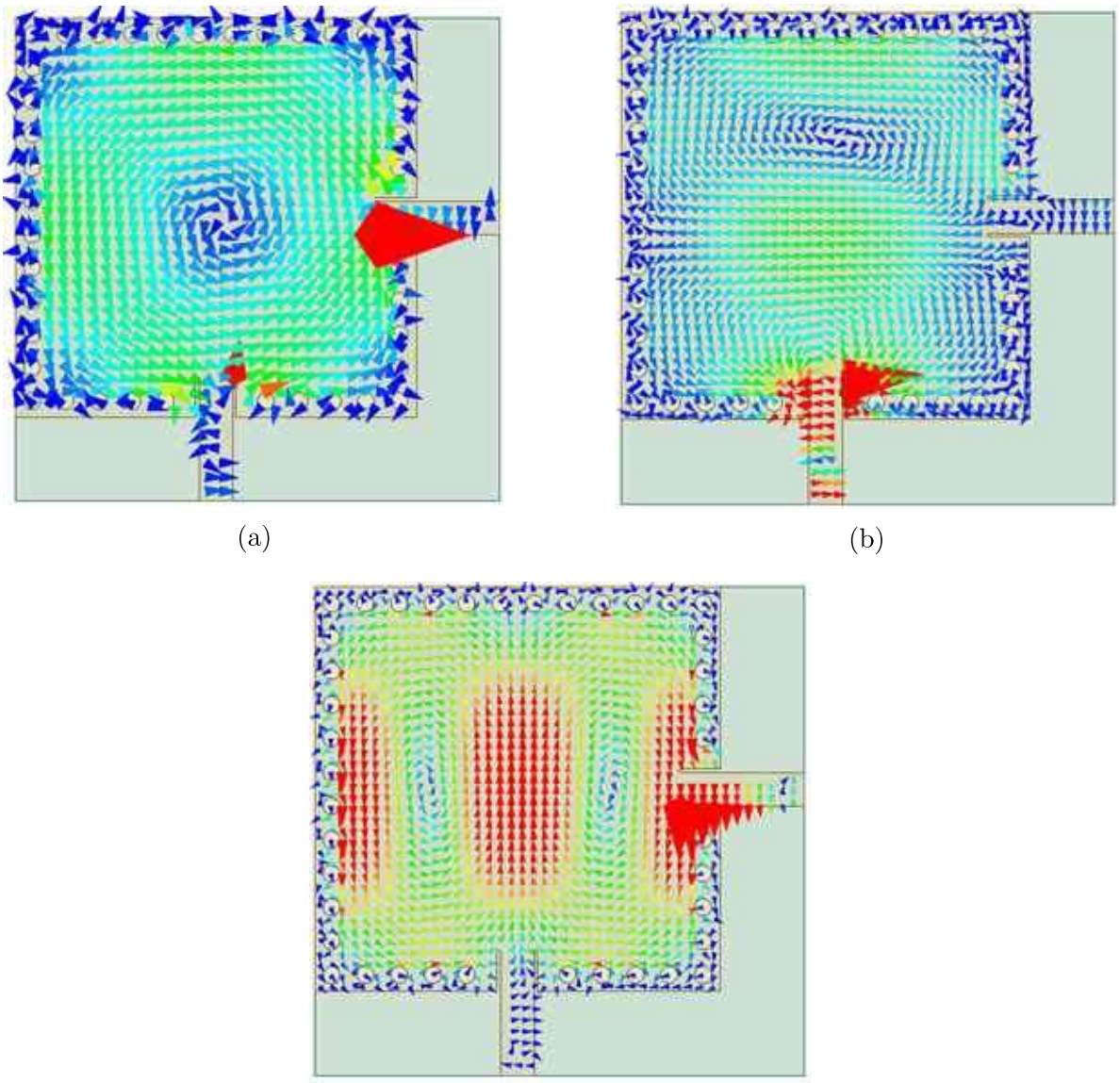

(a) (b)

(c)

Figure 4.13: Vector H-field distribution of SIW cavity without any slot at (a) 6.88 GHz when only port-1 is ON (TE_{110}), (b) 10.89 GHz when only port-1 is ON (TE_{120}) and (c) 10.89 GHz when only port-2 is ON (TE_{210}).

$$W_{cav,eff} = W_{cav} - 1.08\frac{d_V^2}{p_V} + 0.1\frac{d_V^2}{W_{cav}} \tag{4.6c}$$

where ε and μ are the permittivity and permeability of the dielectric material used whereas m, n and p are the integers (=1, 2, 3,...) and denote the number of variations in the standing wave pattern corresponding to x-, y- and z-axis directions. For a square SIW cavity, i.e., $L_{cav,eff}$=$W_{cav,eff}$ and $m \neq n$, several orthogonal degenerate modes will start propagating inside the SIW cavity as shown in Fig. 4.13. When the square SIW cavity is fed with port-1 only (port-2 is terminated by 50Ω matched load), the TE_{110} and TE_{120} modes are excited at 6.88 GHz and 10.89 GHz as shown in Fig. 4.13(a) and 4.13(b), respectively. Similarly, the TE_{210} mode at 10.89 GHz as shown in Fig. 4.13(c) is excited inside the same cavity when fed from port-2 only (port-1 is terminated by 50Ω load).

4.2.1.2 Self-diplexing operation

The hexagonal slot along with the two rectangular slots are not etched exactly at the center of the SIW cavity, i.e., the asymmetric placement of the hybrid-slot divides the whole SIW cavity into two fictitious asymmetric SIW cavities. As a result, two distinct frequency bands centered around 5.23 GHz and 7.50 GHz start resonating inside the SIW cavity when excited individually. Due to loading of the hybrid slot, the original TE_{110} and TE_{210} resonant modes get perturbed and new cavity modes with lower resonant frequency, i.e., at 5.23 and 7.50 GHz are generated. The vector H-field distribution at 5.23 GHz and 7.50 GHz resonating modes are illustrated in Fig. 4.14(a) and 4.14(b), respectively. A different current paths are created by TE_{210}/TE_{120} and TE_{110} modes propagating inside SIW cavity due to field concentration near port-1 and port-2, respectively. This results into creation of single transmission zero (TZ) around 7 GHz (as depicted by a dip in the isolation graphs discussed in next sub-sections) which lies between the two resonances, i.e., 5.23 and 7.50 GHz.

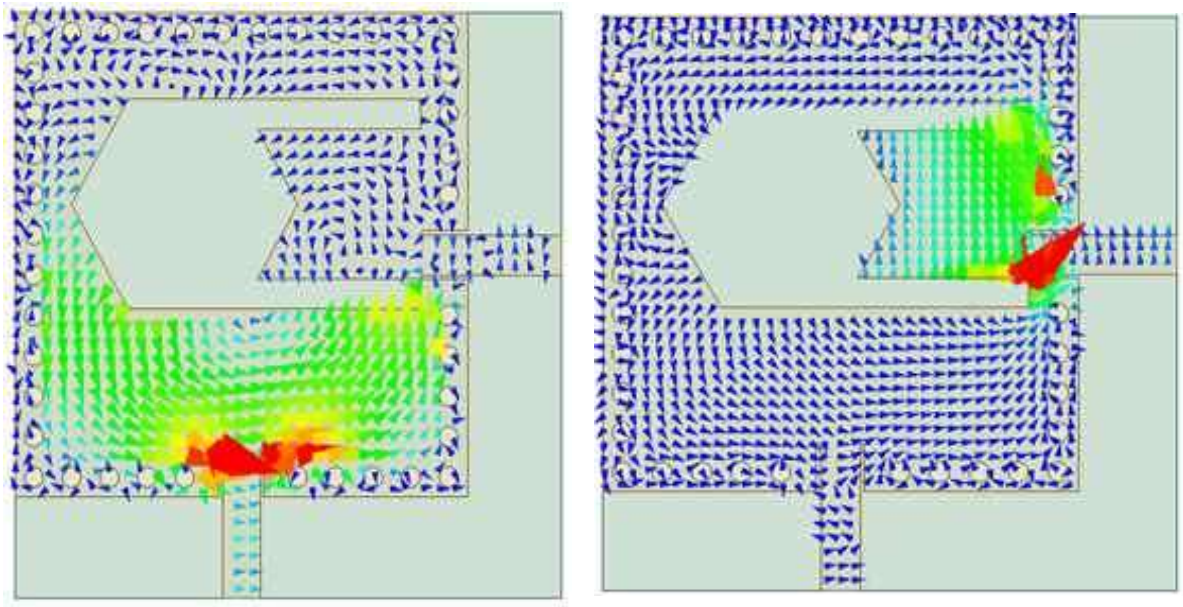

(a) (b)

Figure 4.14: Vector H-field distribution with hybrid slot at (a) 7.50 GHz when only port-1 is ON (TE_{210}) and (b) 5.23 GHz when only port-2 is ON (TE_{110}).

4.2.1.3 Effect of NLR and frequency tunability

The concept of NLR was first discussed in [172] where three different NLRs, i.e., elongation, cutting and distortion (or re-grouping) were discussed for obtaining desired flexibility in the radiation pattern of fractal antennas. Reference [173] utilizes elongation NLR on Sierpinski Knopp wide-slot structure for tri-band operation. On similar lines, elongation NLR is applied on the hexagonal slot and its effect of lower and upper resonant frequency is studied. Fig. 4.15 illustrates a basic NLR steps in a regular hexagon where scaling in x- and y-directions is regulated by two parameters, namely x_{scale} and y_{scale}, respectively. When there is no scaling in any direction, both x_{scale} and y_{scale} takes value equals to 1. With (x_{scale} >1, y_{scale}=1) and (y_{scale} >1, x_{scale}=1), there will be scaling in x- and y-directions, respectively.

The operating frequency of the proposed SDA with hybrid slot can be tuned independently by just varying the scaling parameters, i.e., x_{scale} and y_{scale} which makes the

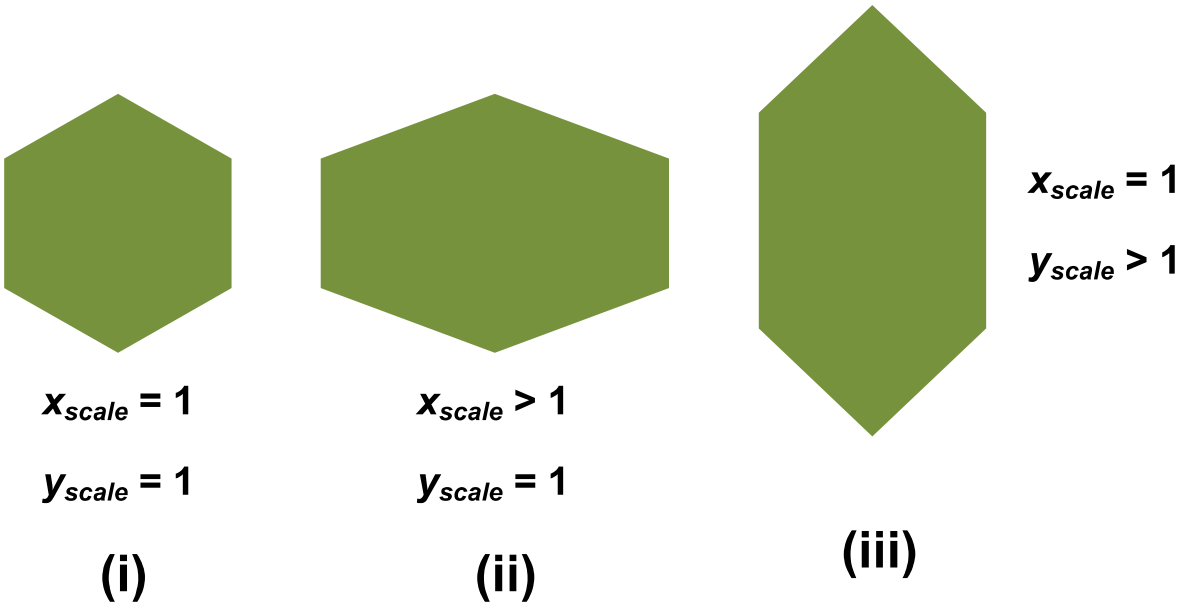

Figure 4.15: Hexagonal slot showing scaling as NLR in (i) no direction, (ii) x-direction only and (iii) y-direction only.

design more flexible for SDA operation. Fig. 4.16(a) illustrates the tuning of 7.50 GHz frequency band when x_{scale} is varied from 1.0 to 1.4 keeping y_{scale}=1. With 1.0 $\leq x_{scale} \leq$ 1.4, the resonating second operating frequency is shifted from 7.37 to 7.81 GHz due to decrease in capacitive loading while no significant variation in first operating frequency is noticed. Also, the isolation between the two ports gets from average 44.71 to 50.02 dB with variation in x_{scale} from 1.0 to 1.4, respectively.

Similarly, when y_{scale} is varied from 1.0 to 1.4, the first operating frequency changes from 5.29 to 5.53 GHz due to decrease in capacitive loading with minimal change in second operating frequency as shown in Fig. 4.16(b). The average isolation with 1.0 $\leq y_{scale} \leq$ 1.4 goes from 44.71 to 49.36 dB.

4.2.1.4 Self-triplexing operation

To obtain the self-triplexing operation, a parasitic hexagonal patch (similar to hexagonal slot) is placed concentrically inside the hexagonal slot. This parasitic hexagonal patch is excited by coaxial probe. Due to this configuration, the antenna now able to radiate at

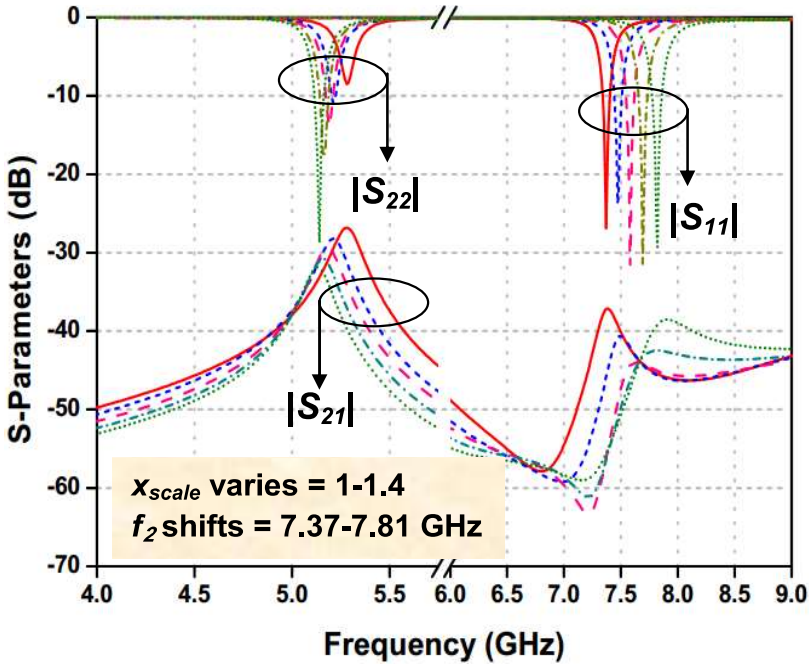

(a)

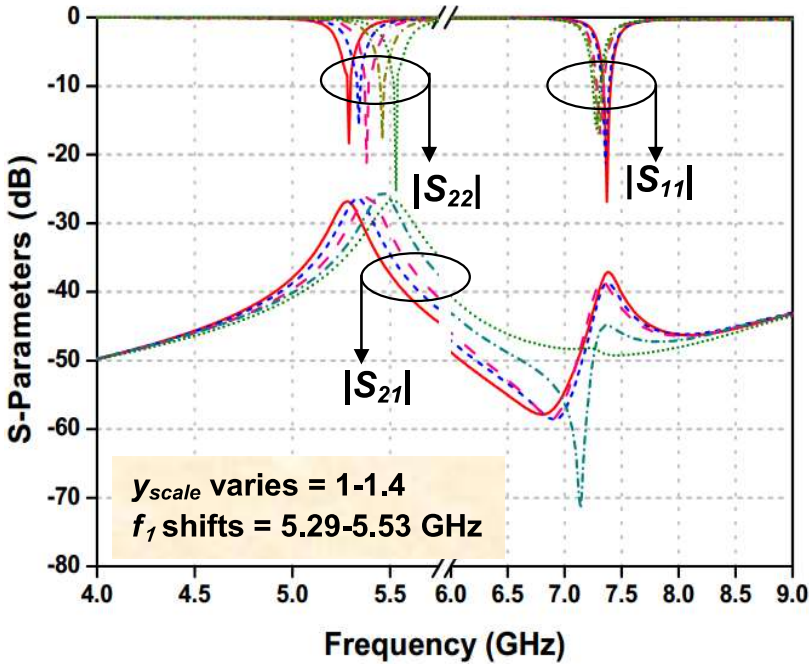

(b)

Figure 4.16: Independent frequency reform at (a) port-1 and (b) port-2 with x_{scale} (keeping y_{scale} constant, equals to 1) and y_{scale} (keeping x_{scale} constant, equals to 1), respectively. Shift in resonating frequency corresponding to parameter are noted in each figure.

three different frequencies. The variation in the gap between the hexagonal patch and similar parasitic patch (or g) changes the coupling capacitance between them through dielectric region (C_{gd}) and through air (C_{ga}) that in turn changes the third resonating frequency around 10.82 GHz. The expressions for coupling capacitances C_{gd} and C_{ga} can be given by [157]:

$$C_{gd} = (\frac{\varepsilon_r \varepsilon_0}{\pi}) ln\{coth(\frac{\pi g}{4h})\} + 0.65 C_f [\frac{0.02}{g/h}\sqrt{\varepsilon_r} + 1 - \frac{1}{\varepsilon_r^2}] \tag{4.7a}$$

$$C_{ga} = \frac{1}{2}\varepsilon_0 \frac{K(k')}{K(k)} \tag{4.7b}$$

where $k = \frac{g}{g+2w}$, $k' = \sqrt{1-k^2}$ and

$$\frac{K(k')}{K(k)} = \begin{cases} \frac{1}{\pi} ln(2\frac{1+\sqrt{k'}}{1-\sqrt{k'}}) & 0 \leq k \leq 0.5 \\ \frac{\pi}{ln[2(\frac{1+\sqrt{k}}{1-\sqrt{k}})]} & 0.5 \leq k \leq 1 \end{cases}$$

The independent tuning of the third operating frequency (f_{r3}) can be explicated by varying the parameter g. The change in g from 0.5 mm to 2.5 mm brings corresponding shift in f_{r3} from 10.82 GHz to 13.45 GHz due to increase in coupling capacitances as illustrated in Fig. 4.17(a). The port-3 exciting the parasitic hexagonal patch is placed asymmetric to both port-1 and port-2 which creates two TZs (TZ-1 in $|S_{31}|$ and TZ-2 in $|S_{21}|$) which improves the isolation of both port-1 and port-2 with port-3 (see Fig. 4.17(b)). The vector H-field distribution when the proposed STA is excited with port-3 only (keeping other ports terminated with 50Ω matched load) is shown in Fig. 4.17(c). It is seen that the proposed STA shows TE_{110} at 10.7 GHz with maximum intensity at the parasitic hexagonal patch only. In short, the features of the proposed STA can be concluded as following:

1. It operates at three different frequencies, i.e., f_{r1}=5.23 GHz, f_{r2}=7.50 GHz and f_{r3}=10.82 GHz. Independent tuning of the resonating frequencies is also possible.

2. Two TZs, one near 5.5 GHz in $|S_{31}|$ and other near 7 GHz in $|S_{21}|$ are generated due to orthogonal placement of the port-1 and port-2.
3. High isolation (>40 dB) among all the three ports is achieved due to their asymmetric and orthogonal placement with respect to each other.

The graphs showing shift in resonant frequency and their ratio(s) against parameters x_{scale}, y_{scale} and g affecting resonating frequencies f_{r1}, f_{r2} and f_{r3}, respectively are plotted in Fig. 4.18. This indicates that the each frequency ratios can be adjusted over a certain region as per the requirement.

Table 4.2: tunable ranges of operating frequencies and supporting applications

Parameter Range	**Frequency Range (GHz)**	**Supporting Applications**
1.0 $\leq x_{scale} \leq$ 1.4	7.38 $\leq f_{r2} \leq$ 7.81 (Port-1)	LTE/LTE-Advanced, WLAN, and metrological satellite for weather monitoring
1.0 $\leq y_{scale} \leq$ 1.4	5.29 $\leq f_{r1} \leq$ 5.53 (Port-2)	WLAN and Wi-Fi
0.5 $\leq g \leq$ 2.5	10.82 $\leq f_{r2} \leq$ 13.45 (Port-3)	Amateur radio and amateur satellite operations

4.2.1.5 Equivalent Circuit Model

Fig. 4.19(a) portrays the equivalent circuit of the SIW based STA, where each cavity mode is modelled as a parallel combination of R, L and C elements. The coupling between the feed and cavity can be modelled as a transformer with a shunt reactance and turns-ratio 1:n. The Circuit Design component of the ANSYS Electronics Desktop software (ver. 17.2) was used for optimizing the equivalent circuit model. The return

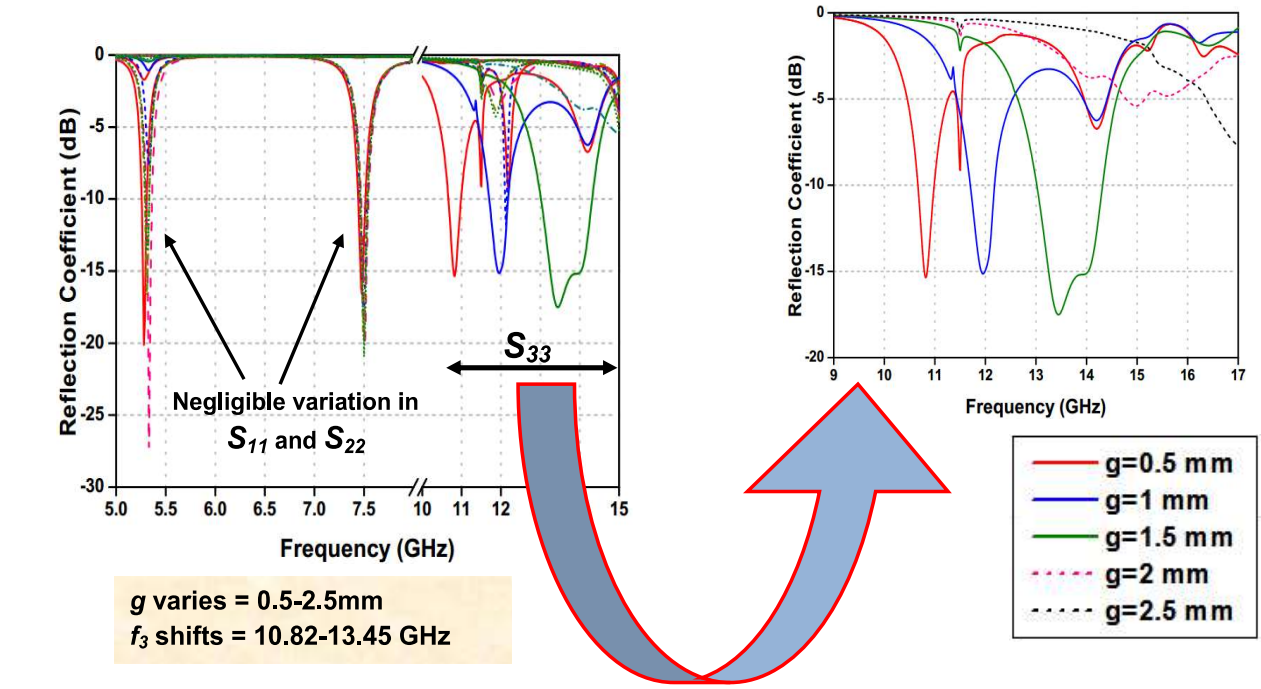

(a)

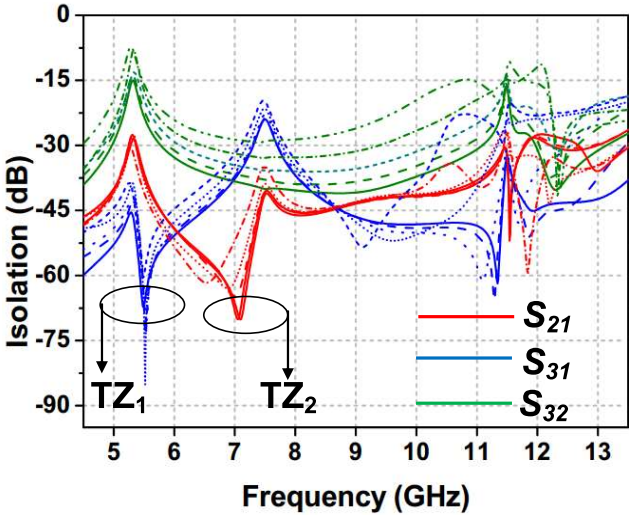

(b)

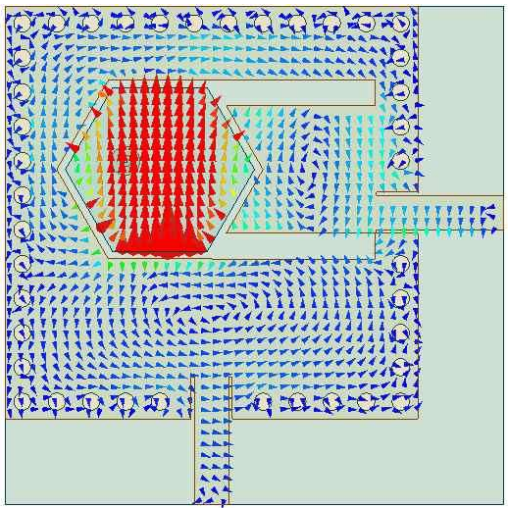

(c)

Figure 4.17: Tuning of third resonating frequency with varying values of g.

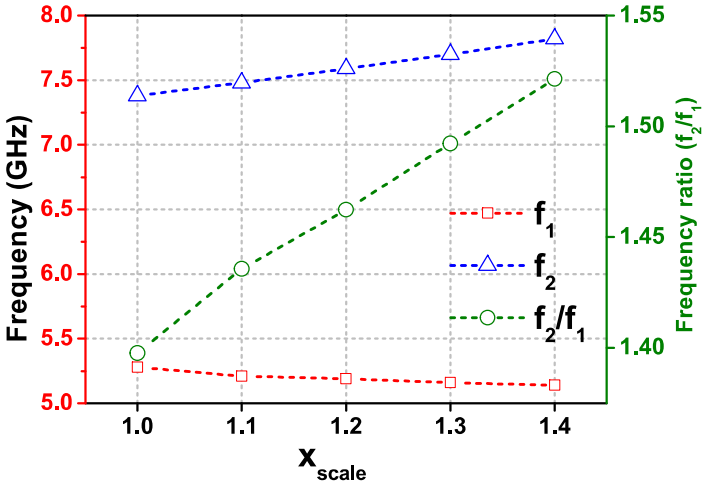

(a)

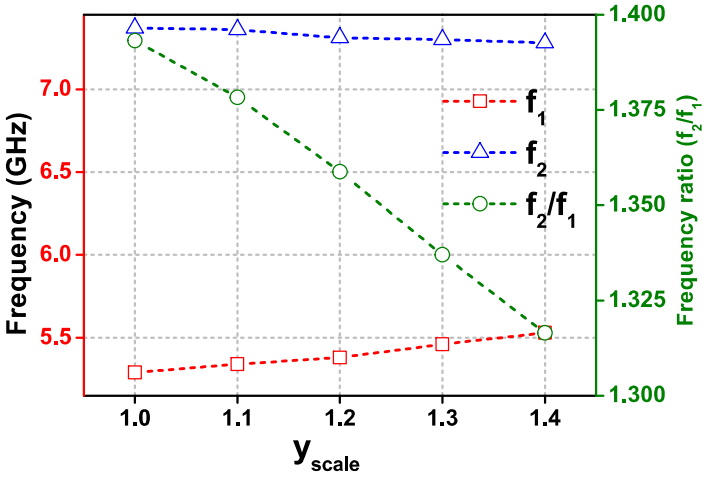

(b)

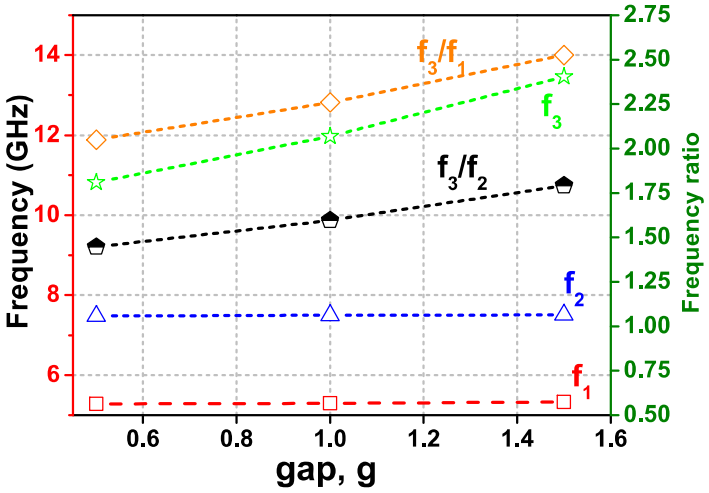

(c)

Figure 4.18: Variation in resonating frequencies f_{r1}, f_{r2} and f_{r3} against parameters (a) x_{scale}, (b) y_{scale} and (c) gap, g, respectively.

loss (S_{11}) of the equivalent circuit model at each resonating frequency is compared with the equivalent circuit model in Fig. 4.19(b).

4.2.2 Experimental Validation

In order to support the idea of SIW-based triple-band STA, a prototype of the proposed antenna is fabricated as shown in Fig. 4.20(a) and 4.20(b). The fabricated STA is characterized for validation and tested experimentally as shown in Fig. 4.20(c) and 4.20(d). Three low loss connectors are connected and soldered at three excitation ports and the measurement related to return losses ($S_{11}/S_{22}/S_{33}$) and isolation ($S_{21}/S_{31}/S_{32}$) is performed using Vector Network Analyzer (Agilent Technologies N5247A). The simulated and measured coefficients at all three ports are shown in Fig. 4.21(a). When excited with port-1, port-2 and port-3 individually (keeping other two ports terminated with 50Ω matched load), the measured (simulated) resonating frequencies f_{r1}, f_{r2}, and f_{r3} are 5.33 GHz (5.23 GHz), 7.53 GHz (7.50 GHz), and 11.02 GHz (10.82GHz) which are in acceptable limits. The isolation between the excitation ports, i.e., S_{21}, S_{31}, and S_{32} are also measured which are also found in good agreement with the simulated ones as illustrated in Fig. 4.21(b).

The gain and far-field measurement are performed inside the anechoic chamber with measurement setup as shown in Fig. 4.22(a). The measured (simulated) peak gain values are 7.33 (7.65) dBi, 6.66 (6.93) dBi, and 6.28 (6.74) dBi at lower band, middle band, and upper frequency bands, respectively as reported in Fig. 4.22(b). It is noted that gain within a particular frequency band is obtained by applying excitation at only one port while terminated other two ports with matched 50Ω. The slight variations between simulated and measured values can be attributed to the soldering joints, uncontrolled dielectric losses, and fabrication imperfections. The value of tolerances for simulated vs. experimental resonating frequencies of the proposed antenna are ±0.93% for port-1, ±0.66% for port-2, and ±1.6% for port-3.

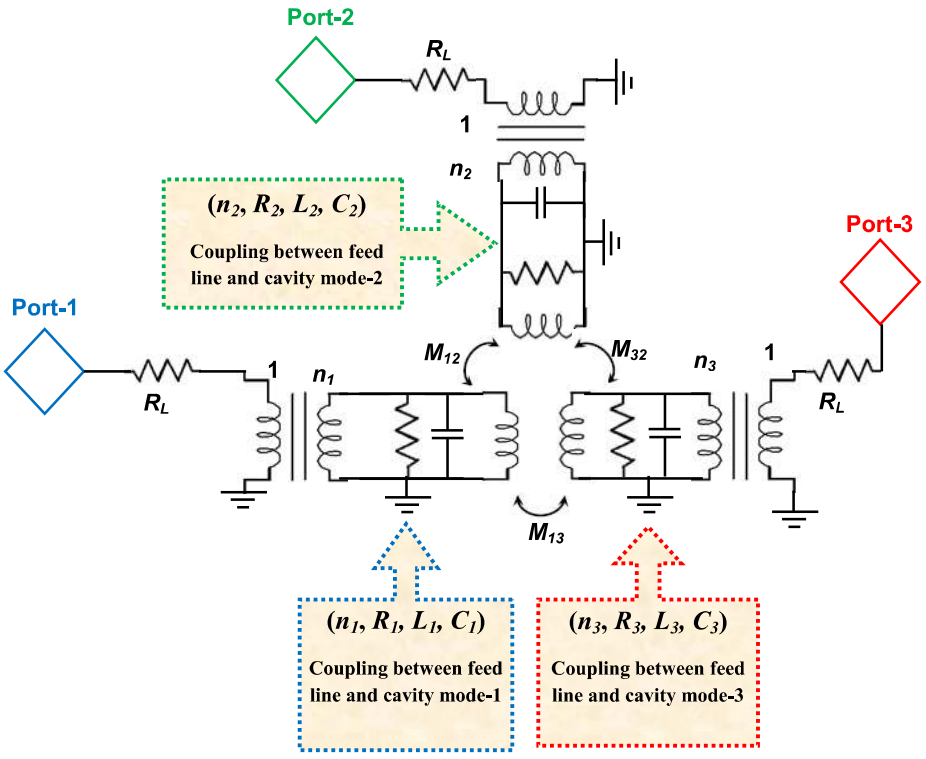

(a)

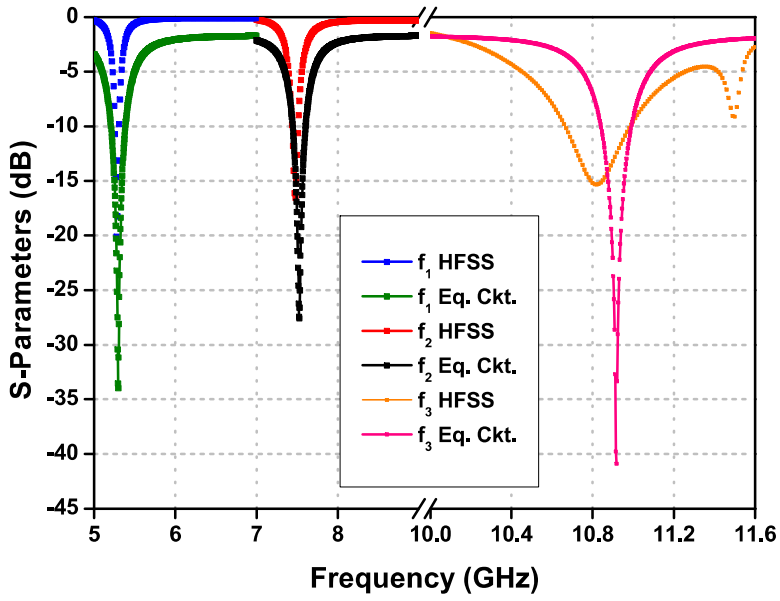

(b)

Figure 4.19: Independent frequency reform at (a) port-1 and (b) port-2 with x_{scale} (keeping y_{scale} constant, equals to 1) and y_{scale} (keeping x_{scale} constant, equals to 1), respectively. Shift in resonating frequency corresponding to parameter are noted in each figure. The modal parameters are: n_1=3.18, R_1=478Ω, L_1=0.629 nH, C_1=1.4349 pF, n_2=6.172, R_2=1.89 KΩ, L_2=1.08 nH, C_2=0.414 pF, n_3=8.37, R_3=3.13 KΩ, L_3=0.793 nH, C_3=0.293 pF.

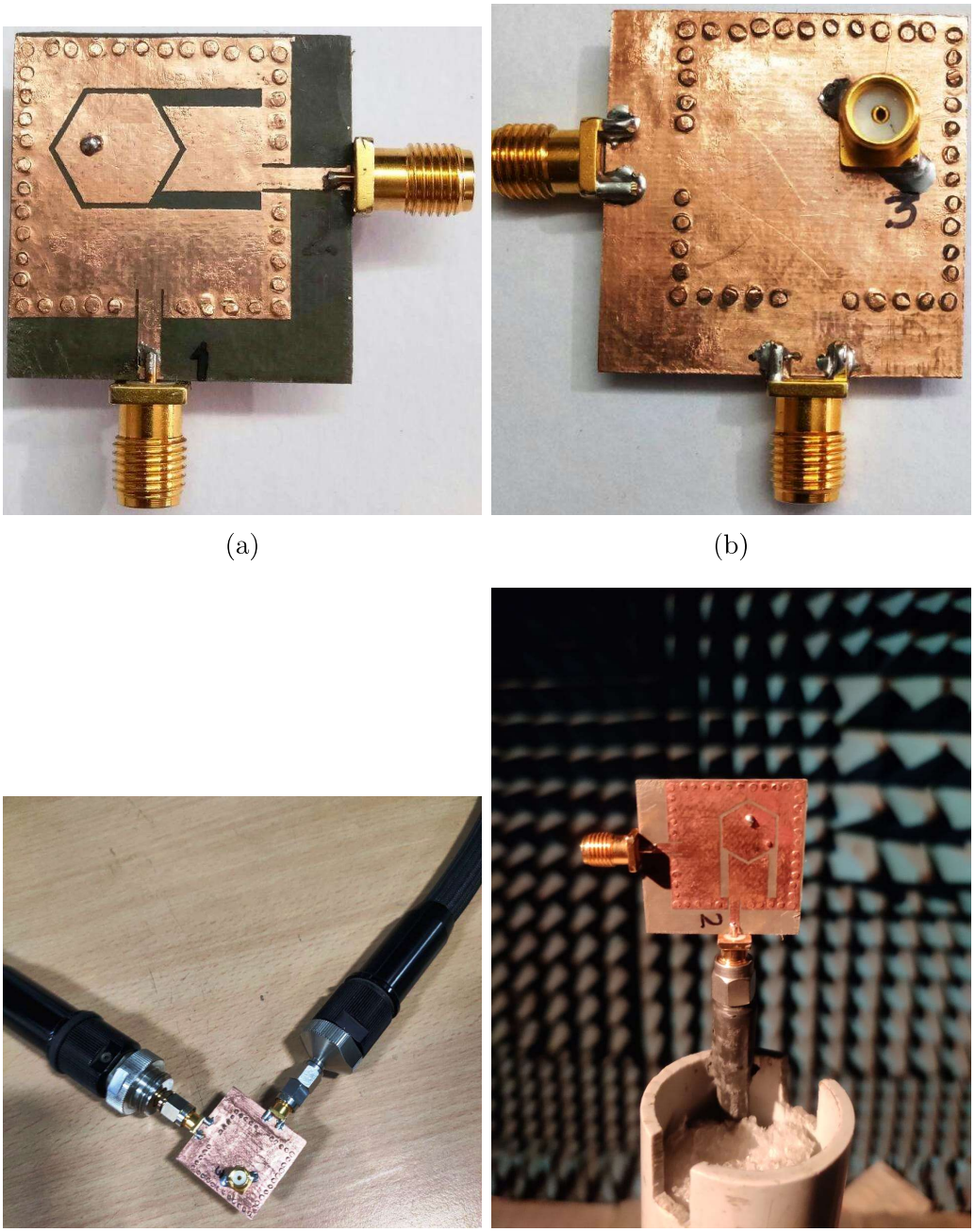

(a) (b)

(c) (d)

Figure 4.20: Fabricated prototype of the proposed STA (a) front side, (b) back side, (c) testing during VNA and (d) inside anechoic chamber for gain/efficiency and radiation pattern measurement.

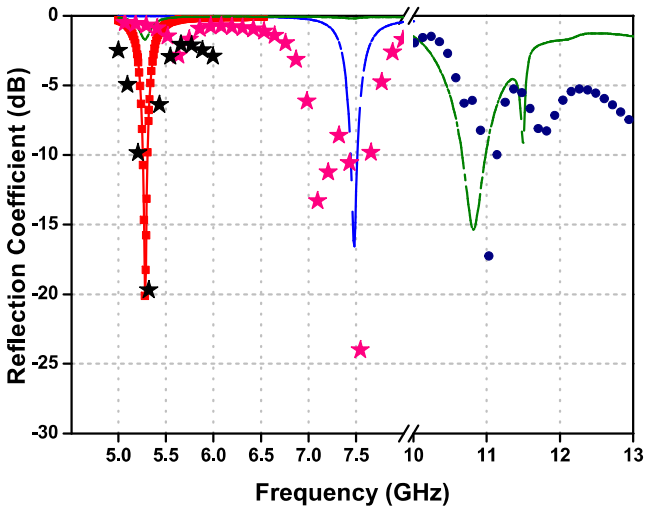

(a)

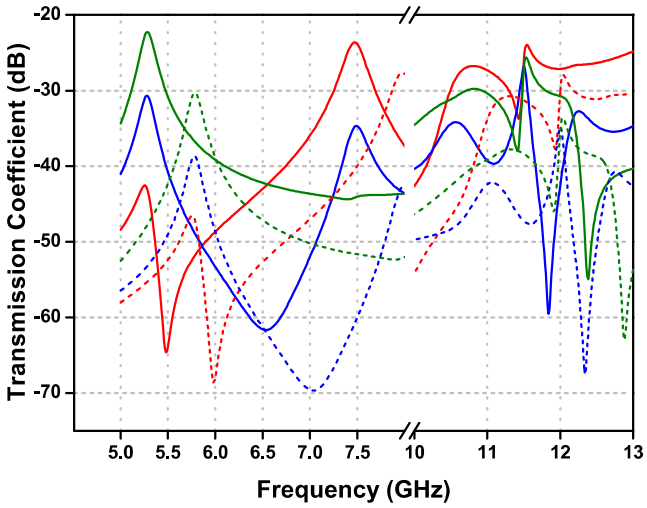

(b)

Figure 4.21: Comparison of simulated (solid line) and measured (dashed line) (a) reflection coefficient and (b) S_{21}(red), S_{31}(blue), S_{32}(green).

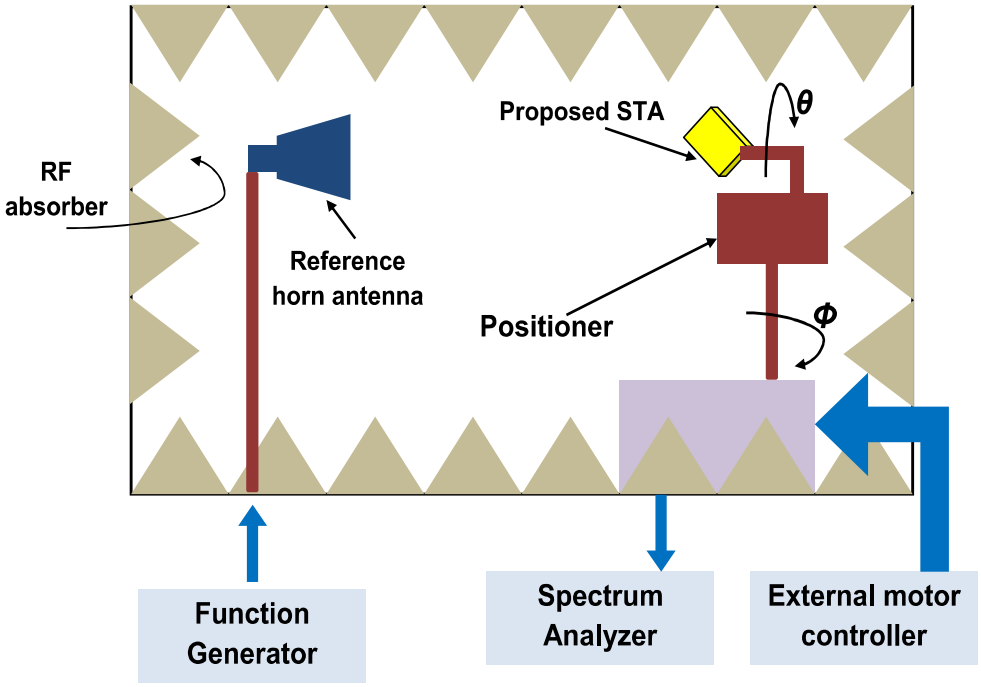

(a)

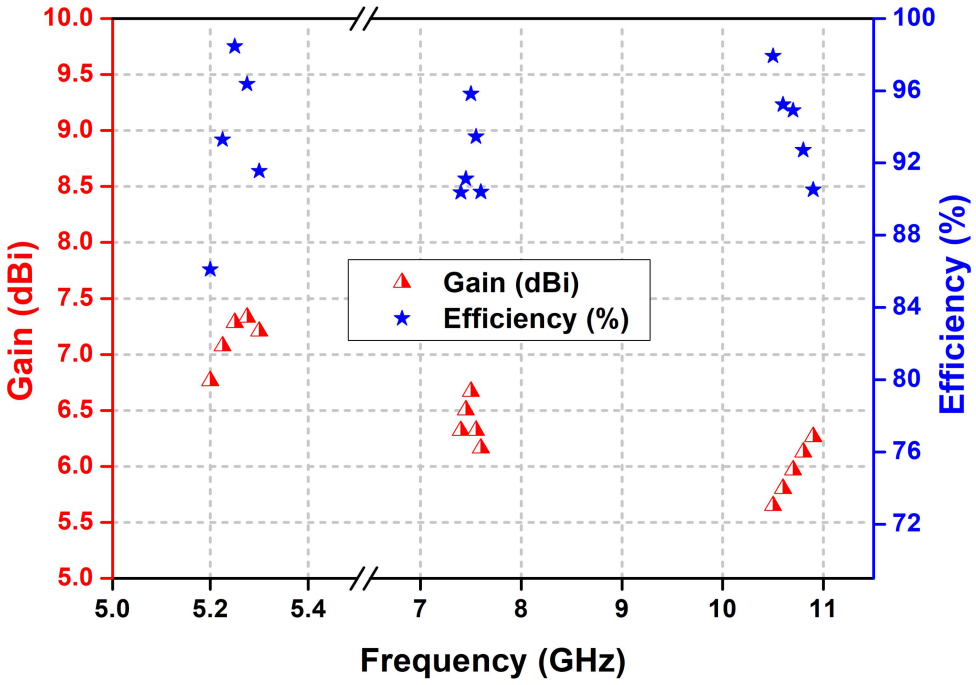

(b)

Figure 4.22: (a) Gain and radiation pattern measurement set-up sketch and (b) measured gain/efficiency of the triplexing antenna.

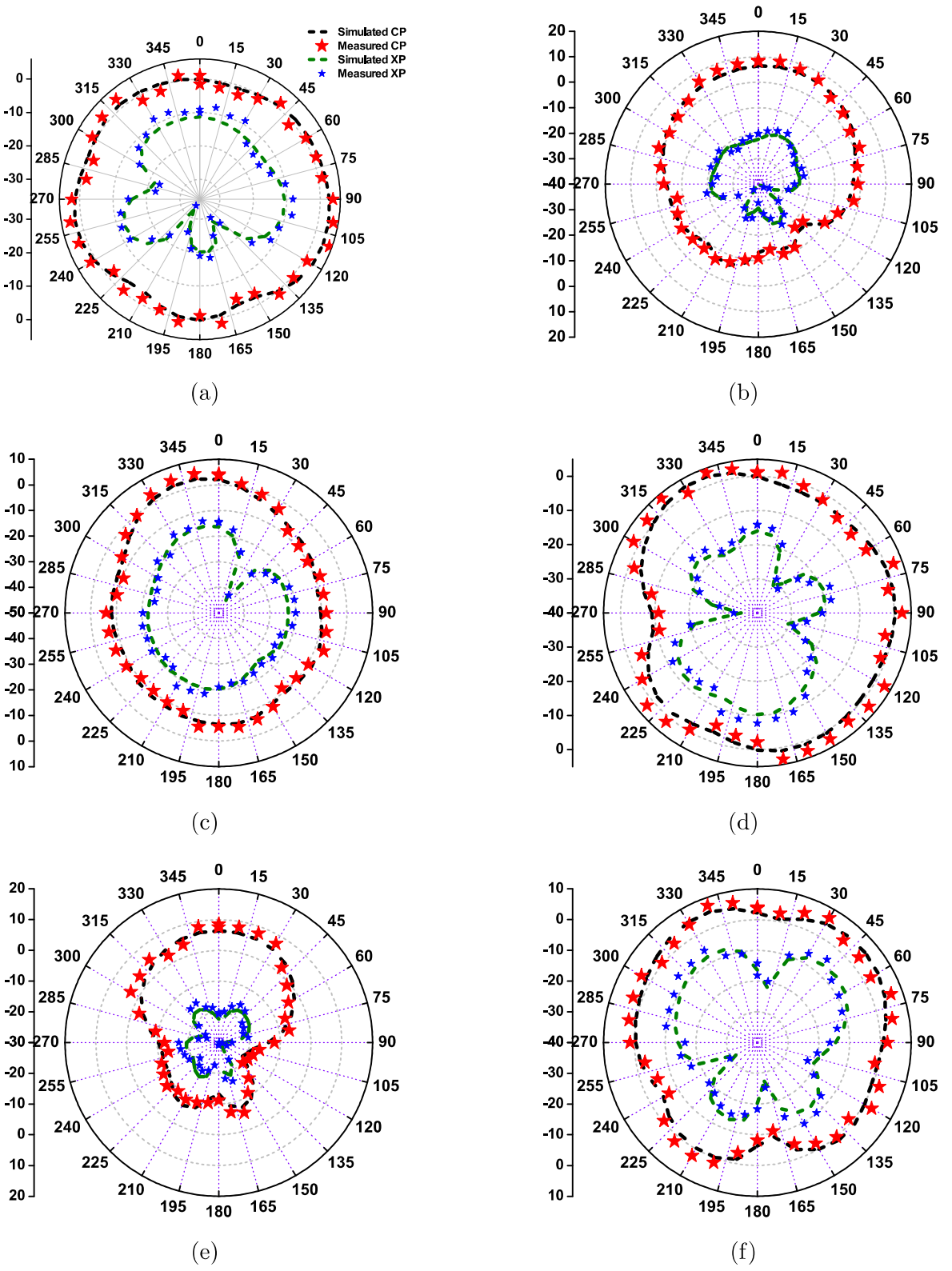

Figure 4.23: Simulated (solid line) and measured (dotted line) radiation patterns of the proposed STA. *E*-plane at (a) 5.33 GHz, (b) 7.53 GHz and (c) 11.02 GHz and *H*-plane at (d) 5.23 GHz, (e) 7.53 GHz and (f) 11.02 GHz.

Table 4.3: performance comparison with existing SIW-based STAs

Reference	Physical Size (mm^2)	Electrical Size	Resonant frequency (GHz)	Isolation (dB)	Gain (dBi)	FTBR (dB)	Slot shape
[100]	23×32	$0.5\lambda_o^2$	7.89/9.44/9.87	22.5	7.2	17.3	Bow-tie
[102]	60×44	$1.08\lambda_o^2$	4.18/5.2/5.8	42/23.7/22.5	6.56/4.2/5.85	19	One annular slot and two transverse slots
[103]	-	$0.69\lambda_o^2$	3.5/4.8/5.4	26	4.5/5.9/6	16.1/18.5/22.8	One annular slot and two transverse slots
[104]	34.5×29.10	$0.42\lambda_o^2$	6.53/7.65/9.09	19	3.1/4.7/3.9	13.2	T-shape
[105]	48×48		5.6/6.64/6.95	23.8	-	-	T-shape
[106]	12.6×26.9	$0.08\lambda_o^2$	4.95/5.3/5.9	20.5	4.5/4.9/6.1	14	Inverted V-shape
[107]	32×32	$0.17\lambda_o^2$	4.14/6.1/8.32	30.8/31.4/34.2	4.26/4.41/6.27	15/16/20	Modified I-shape
[101]	-	-	6.77/8.57/13.37	15.6/23/17	4.67/5.15/5.8	14	Dumbbell shape
This work	29×29	$0.25\lambda_o^2$	5.23/7.50/10.82	43.27/47.84/45.17	7.33/6.66/6.28	25.46/28.17/32.59	NLR hexagonal patch with two rectangular narrow slots

The simulated and measured radiation patterns for three operating frequency bands (5.33, 7.53 and 11.02 GHz) in two orthogonal planes (ϕ=0° and ϕ=90°) are compared in Fig. 4.23. In both ϕ=0° and ϕ=90° planes, the co-polarization to cross-polarization difference for all resonating frequencies is ≥16.5 dB. It is seen that the measured responses are consistent with the simulated ones for the proposed STA. A little deviation between the two is observed which is probably due to the fixing of SMA connector and fabrication tolerances. In the similar manner, the FTBR reported in all three bands is better than 25 dB. This makes the proposed STA a suitable candidate for applications that falls within the below frequency ranges, as listed in Table 4.2.

Table 4.4: Simulated and (measured) results of proposed STA

Parameters \ Excitation	Excitation Port		
	Port-1	**Port-2**	**Port-3**
Resonating frequency (GHz)	5.33 (5.28)	7.53 (7.48)	11.02 (10.81)
10 dB bandwidth (MHz)	50 (47)	71 (69)	310 (304)
Isolation (dB)	>40	>40	>40
Gain (dBi)	7.33 (7.65)	6.66 (6.93)	6.28 (6.74)
FTBR (dB)	25.46	28.17	32.59
Efficiency (%)	97.39	95.82	97.83

The advantages of the proposed STA highlighted in Table 4.3. Here, a detailed comparative study with the already proposed STAs in the literature in terms of physical/electrical size, isolation, gain, efficiency, FTBR and complexity is summarized. The proposed STA possesses compact size along with high isolation among the ports and good gain/efficiency levels than the existing literature.

In this chapter, two novel designs of SIW cavity-backed self-diplexing and self-triplexing antenna are presented. First, a compact self-diplexing circularly polarized (CP) SIW antenna with an elliptical slot is presented. Initially, an elliptical slot is etched in the metallic ground plane, and its proper positioning (i.e., distance d_s) helps in achieving dual-band operation, i.e., centered around 21 GHz and 28 GHz. The rotation

of the elliptical slot helps in producing two orthogonal electric field vectors of almost equal amplitude and phase difference of 90°, thereby achieves CP operation in both frequency bands. Proper tuning of elliptical slot dimensions and rotation angle are the two factors that affect the 3 dB axial-ratio bandwidth (ARBW) of the proposed antenna. Measured results show that the proposed antenna exhibits dual-band operation in 21.38-21.92 GHz (2.49%) and 26.68-27.58 GHz (3.32%) along with corresponding ARBW of 21.25-21.90 GHz (3.01%) and 27-28.85 GHz (6.62%), respectively. Due to the SIW cavity, the proposed antenna shows a unidirectional radiation pattern with a gain more than 5 dBic and isolation better than 22 dB in both the frequency bands. This makes the proposed antenna an attractive/suitable candidate for both satellite broadcasting and 5G applications.

Next, a compact SIW cavity backed antenna with enhanced self-triplexing property is presented. The designed antenna supports operation in three different frequency bands, i.e., 5.23, 7.50 and 10.82 GHz simultaneously. The proposed design comprised of single SIW cavity loaded with hexagonal slot merged with two rectangular narrow slots. Initially, the fundamental TE_{110} mode along with two degenerated TE_{120} and TE_{210} modes are excited inside the SIW cavity with the help of orthogonally placed microstrip feed lines. Due to slot loading, the fundamental mode along with degenerate modes shift towards lower frequency, leading to overall size compactness of 68% as compared to [102]. Up to this stage, the proposed design supports two frequency bands centered around 5.23 and 7.50 GHz. For self-triplexing operation, a parasitic patch (similar to hexagonal slot) is placed concentrically inside it. This enabled the antenna to work in 10.82 GHz frequency band as well. The proposed self-triplexing antenna allows independent tuning of all three frequency bands using a single parameter/variable. High isolation among the excitation ports ($>$ 40 dB), good gain level ($>$ 6 dBi), high FTBR ($>$ 25 dB), and compact size ($0.25\lambda_o^2$) make the proposed triplexer a preferable candidate for both C- and X-band applications including WLAN/5G/WiMAX/Wi-Fi,

amateur radio and satellite operations.

The use of self-diplexing antennas, as detailed in this chapter, results in a low-profile RF front-end by removing the need for complex diplexers within the circuit. On the other hand, multiple-input-multiple-output (MIMO) technology has emerged as an essential component of the next generation of wireless communication systems, as MIMO antennas may considerably improve data rates while maintaining the same bandwidth and power level. Previously reported SIW-based MIMO antennas in the literature occupy a larger area, making them incompatible with future-generation wireless devices. Furthermore, very few of those reported antennas offer good isolation across all the operating bands. There is potential to develop a miniaturised planar multi-band SIW-based MIMO antenna with strong isolation (at least better than 15 dB) and performance across all communication frequency bands. In the next chapter, a design of compact Multiple-Input Multiple-Output Dual-band Dual-Circularly Polarized SIW Cavity-Backed Slot Antenna for Satellite and 5G Systems are proposed.